

Hybrid Angle Control and Almost Global Stability of Grid-Forming Power Converters

Ali Tayyebi, Adolfo Anta, and Florian Drrler

Abstract—This paper introduces a new grid-forming control for power converters, termed hybrid angle control (HAC) that ensures the almost global closed-loop stability. HAC combines the recently proposed matching control with a novel nonlinear angle feedback reminiscent of (though not identical to) classic droop and dispatchable virtual oscillator controls. The synthesis of HAC is inspired by the complementary benefits of the dc-based matching and ac-based grid-forming controls as well as ideas from direct angle control and nonlinear damping assignment. The proposed HAC is applied to a high-fidelity nonlinear converter model that is connected to an infinite bus or a center-of-inertia dynamic grid models via a dynamic inductive line. We provide insightful parametric conditions for the existence, uniqueness, and global stability of the closed-loop equilibria. Unlike related stability certificates, our parametric conditions do not demand strong physical damping, on the contrary they can be met by appropriate choice of control parameters. Moreover, we consider the safety constraints of power converters and synthesize a new current-limiting control that is compatible with HAC. Last, we present a practical implementation of HAC and uncover its intrinsic droop behavior, derive a feedforward ac voltage and power control, and illustrate the behavior of the closed-loop system with publicly available numerical examples.

Index Terms—grid-forming converter control, current-limiting control, power system stability, hybrid angle control.

I. INTRODUCTION

The Generation technology in power system has been drastically changing in recent years. The increasing replacement of bulk synchronous generators (SG) with converter-interfaced generation is transforming the power system to a so-called *low-inertia* system. The stability aftermath of this transition is highlighted by significant inertia reduction, fluctuating actuation (i.e., volatile generation), and the potential adverse interactions due to the presence of adjacent timescales [1]–[7], among others. The *grid-forming* control concept is envisioned to address the aforementioned stability challenges, whereby the converter features frequency and voltage regulation, black-start, and load-sharing capabilities [8].

Several grid-forming control techniques have been recently proposed. *Droop control* mimics the speed droop of SG, controls the modulation angle proportional to the active power imbalance, and is widely recognized as the baseline solution [9],

A. Tayyebi (the corresponding author) is with the Austrian Institute of Technology, 1210 Vienna, Austria, and also with the Automatic Control Laboratory, ETH Zurich, 8092 Zurich, Switzerland, e-mail: ali.tayyebi-khameneh@ait.ac.at.

A. Anta is with the Austrian Institute of Technology, 1210 Vienna, Austria, e-mail: adolfo.anta@ait.ac.at.

F. Drrler is with the Automatic Control Laboratory, ETH Zurich, 8092 Zurich, Switzerland, e-mail: dorfler@ethz.ch.

This work was partially funded by the independent research fund of the Austrian Institute for Technology, and ETH Zurich funds.

[10]. As a natural extension of droop control, the emulation of SG dynamics and control led to *virtual synchronous machine* (VSM) strategies [11], [12]. The recently proposed *matching* control exploits structural similarities of the converter and SG; and matches their dynamics by controlling the modulation angle according to the dc voltage [13]–[17]. Furthermore, *virtual oscillator control* (VOC) mimics the dynamical behavior of Liénard-type oscillators and *globally* synchronizes a converter-based network [18], [19]. Recently, *dispatchable virtual oscillator control* (dVOC) is proposed that ensures *almost global* synchronization of a homogeneous network of oscillator-controlled inverters (with simplified dynamics) to pre-specified set-points consistent with the power flow equations [20], [21] (also see [22] for a comparative transient stability assessment of dVOC and droop control).

A comparison of the aforementioned control strategies reveals complementary benefits; see [2, Rem. 2]: dc-based matching techniques are robust with respect to (w.r.t.) the load-induced over-currents and ac-based techniques (droop, VSM, and especially dVOC) have superior transient performance. Here we leverage these complementary benefits and design a *hybrid angle control* (HAC) which combines matching control and a nonlinear angle feedback (reminiscent of, though not identical to, droop control and dVOC) and is inspired by ideas from direct angle control [17] and sign-indefinite nonlinear damping assignment [23], [24]. Our proposed controller *almost globally* stabilizes the closed-loop converter dynamics when connected via an inductive line to either an infinite bus (IB) or a dynamic center-of-inertia (COI) grid model. We provide insightful parametric conditions for the existence, uniqueness, and *almost global stability* of closed-loop equilibria. Last but not least, we take into account the converter *safety constraints*, design a new *current-limiting* control, and investigate its stability in combination with HAC.

In contrast to most other related works, we consider a high-fidelity converter model including an explicit representation of energy source dynamics, the dc bus, LC filter, line dynamics, COI grid dynamics, and the converter set-points. In comparison to related stability certificates [17], [25], [26], our stability conditions do not demand strong physical damping, but they can be met by appropriate choice of control gains.

Moreover, our complementary choice of the angle-dependent terms in the *Lyapunov / LaSalle* function and in the HAC formulation overcomes the analysis obstacles arising from lack of damping in angle state. Finally, we conclude this paper with some extensions, namely: a practical implementation and droop behavior of the HAC is described, a feedforward ac voltage and power control is discussed, and the

behavior of the closed-loop system is explored with publicly available numerical examples [27].

In addition, as an interesting technical contribution in its own right, this paper introduces an offbeat manifold space — the boundary of a *Möbius strip*— for studying the evolution of angle trajectories. A theoretical limitation of all (continuous control) systems with angles evolving on the circle is that they can at best achieve almost global asymptotic stability (AGAS) due to the topological obstruction of the circle [28], which is a recurring theme in many of the aforementioned papers. Here we establish AGAS of the angles on the boundary of a Möbius strip, which results in *global* asymptotic stability of the desired equilibrium when projected on the circle.

The remainder of this paper is structured as follows. Section II describes the model of a converter connected to an IB and introduces the HAC. Section III presents the closed-loop analysis and the main result of this work. Section IV discusses two theoretical extensions: dynamic COI grid model consideration and the design of a current-limiting control for grid-forming converters. Section V presents a practical HAC implementation, a complementary feedforward control, and HAC's droop behavior. Next, we verify the performance of our controller via numerical examples in Section VI. Last, a summary and outlook on future work are given in Section VII.

II. MODEL DESCRIPTION

A. Preliminaries and Notation

In this paper, \mathbb{R} denotes the set of real numbers, $\mathbb{R}_{>0}$ denotes the set of strictly positive real numbers and $\mathbb{R}_{[a,b]} := \{x \in \mathbb{R} : a \leq x \leq b\}$. The unit circle i.e., one-dimensional torus is denoted by \mathbb{S}^1 . For the column vectors $x \in \mathbb{R}^n$ and $y \in \mathbb{R}^m$, $(x, y) := [x^\top, y^\top]^\top \in \mathbb{R}^{n+m}$ denotes the stacked vector, and I is the two-dimensional identity matrix. The vector and matrix of zeros are respectively denoted by 0_n and $0_{n \times m}$. The block diagonal matrix is denoted by $\text{blkdiag}(A_1, \dots, A_n)$. Furthermore, $\|\cdot\|$ denotes the Euclidean norm operator. Last, given $\varphi \in \mathbb{S}^1$ we define $\psi(\varphi) := (\cos(\varphi), \sin(\varphi))$.

In this work, similar to [2], [3], [11], [16] among others, we consider symmetric three-phase electric circuitry assuming identical electrical parameters for all three phases and that all three-phase quantities $z_{abc} := (z_a, z_b, z_c) \in \mathbb{R}^3$ are balanced i.e., $z_a + z_b + z_c = 0$. Under the latter assumption, a three-phase quantity z_{abc} is transformed to the stationary $\alpha\beta$ -frame via magnitude preserving Clarke transformation i.e., $z_{\alpha\beta} = C z_{abc}$ (see Appendix B1 for details). Moreover, the image of $z_{\alpha\beta}$ in direct-quadrature (dq) coordinates that rotate with constant frequency $\omega_f \in \mathbb{R}_{>0}$ and the angle $\theta_f = \omega_f t + \theta_f(0) \in \mathbb{S}^1$ is given by $z = R(\theta_f) z_{\alpha\beta}$ with

$$R(\theta_f) := \begin{pmatrix} \cos(\theta_f) & -\sin(\theta_f) \\ \sin(\theta_f) & \cos(\theta_f) \end{pmatrix}.$$

B. Modeling the Connection of Converter and Stiff Grid

The IB three-phase voltage is defined by

$$v_{b,abc} := v_r (\sin(\theta_b), \sin(\theta_b - 2\pi/3), \sin(\theta_b + 2\pi/3)),$$

where $v_r \in \mathbb{R}_{>0}$ is the nominal ac voltage magnitude, and

$$\theta_b := \omega_0 t + \theta_b(0) \in \mathbb{S}^1 \quad (1)$$

is the IB absolute angle with the nominal frequency $\omega_0 \in \mathbb{R}_{>0}$.

We consider an average model of a three-phase two-level dc-ac converter [29, Chap. 5] and model the dc energy source by a first-order system that provides the input for a controlled dc current source. This is a reasonable coarse-grained model of the dc energy source e.g., see [2, Sec. II.A] [30, Sec. 6.4]. The ac filter is modeled by an LC element. Moreover, the converter is interfaced to the IB with an inductive line (that can also be seen as a low-voltage to medium voltage transformer model); Figure 1 presents a schematic of the overall model.

The dynamical model of the converter-IB system in $\alpha\beta$ -frame is described by (see [16, Sec. II] [29, Chap. 5] for a detailed derivation)

$$\tau_{dc} \dot{i}_{dc} = i_{dc,r} - i_{dc}, \quad (2a)$$

$$c_{dc} \dot{v}_{dc} = i_{dc} - g_{dc} v_{dc} - m_{\alpha\beta}(\mu_r, \theta_c)^\top i_{\alpha\beta}, \quad (2b)$$

$$\ell \dot{i}_{\alpha\beta} = v_{dc} m_{\alpha\beta}(\mu_r, \theta_c) - r i_{\alpha\beta} - v_{\alpha\beta}, \quad (2c)$$

$$c \dot{v}_{\alpha\beta} = i_{\alpha\beta} - g v_{\alpha\beta} - i_{g,\alpha\beta}, \quad (2d)$$

$$\ell_g \dot{i}_{g,\alpha\beta} = v_{\alpha\beta} - r_g i_{g,\alpha\beta} - v_{b,\alpha\beta}, \quad (2e)$$

where τ_{dc} is the source time constant, $i_{dc} \in \mathbb{R}$ is the dc source current, $c_{dc}, v_{dc} \in \mathbb{R}$, and g_{dc} respectively denote the dc-link capacitance, voltage, and the dc conductance (that models the dc-side losses).

Further, $i_{\alpha\beta}, v_{\alpha\beta}$, and $i_{g,\alpha\beta}$ all take values in \mathbb{R}^2 and denote the current flowing through the filter inductance ℓ , the voltage across the filter capacitance c , and the current through the line inductance ℓ_g . Lastly, r, g , and r_g model switching and conduction losses associated with the elements ℓ, c , and ℓ_g , respectively. All parameters take positive and scalar values (due to the three-phase symmetry).

The modulation vector $m_{\alpha\beta}(\mu_r, \theta_c) \in \mathbb{R}_{[-1/2, 1/2]}$ is $m_{\alpha\beta}(\mu_r, \theta_c) := \mu_r \psi(\theta_c)$ with reference magnitude $\mu_r \in \mathbb{R}_{[0, 1/2]}$ and angle $\theta_c \in \mathbb{S}^1$. In what follows, we will use the shorthand m for $m_{\alpha\beta}(\theta_c, \mu_r)$. The reference dc current in (2a) is defined as

$$i_{dc,r} := i_r - \kappa(v_{dc} - v_{dc,r}), \quad (3)$$

where $i_r \in \mathbb{R}$ denotes the open-loop dc current reference, $\kappa \in \mathbb{R}_{>0}$ is the proportional gain of the dc voltage control, and $v_{dc,r}$ is the reference dc voltage. We remark that the forthcoming analysis also applies to the case with energy source being modeled as a stiff voltage source i.e., $\tau_{dc} \rightarrow 0$ and $\kappa \rightarrow \infty$.

C. Hybrid Angle Control and Closed-Loop Dynamics

We synthesize a new grid-forming strategy —hybrid angle control (HAC)— by combining the dc-based matching control (see e.g., [15, Eq. 25]) and a nonlinear angle feedback reminiscent of —though not identical to— droop control and dVOC (see e.g., [10], [22] and Remark 3 for details). Defining the converter relative angle w.r.t. the IB as

$$\theta := \theta_c - \theta_b, \quad (4)$$

the HAC takes the form

$$\dot{\theta}_c = \omega_c := \omega_0 + \eta(v_{dc} - v_{dc,r}) - \gamma \sin\left(\frac{\theta - \theta_r}{2}\right), \quad (5)$$

where $\eta \in \mathbb{R}_{\geq 0}, \gamma \in \mathbb{R}_{> 0}$ are the control parameters and θ_r denotes the reference relative angle (see Proposition 6 on the implicit choice of θ_r via deriving $\psi(\theta_r)$ from given set-points). Since the angle term in the right-hand side (RHS) of (5) is 4π -periodic, the state θ_c evolves on the set $\mathbb{M} := [-2\pi, 2\pi]$ with $\pm 2\pi$ identified with each other. The terminology is due to \mathbb{M} being the boundary of the Möbius strip; see Remark 1 and Figure 2. This geometric curiosity will lead to profound insights later on.

Transforming the ac quantities in (2c)-(2e) to the dq-frame aligned with the IB angle θ_b , we define the state vector

$$x := (\theta, i_{dc}, v_{dc}, i, v, i_g) \in \mathbb{X} := \mathbb{M} \times \mathbb{R}^8 \quad (6)$$

and obtain the overall closed-loop dynamics (2)-(5) as

$$\dot{\theta} = \omega_c - \omega_0 = \eta(v_{dc} - v_{dc,r}) - \gamma \sin((\theta - \theta_r)/2), \quad (7a)$$

$$\tau_{dc} \dot{i}_{dc} = i_r - \kappa(v_{dc} - v_{dc,r}) - i_{dc}, \quad (7b)$$

$$c_{dc} \dot{v}_{dc} = i_{dc} - g_{dc} v_{dc} - m^\top i, \quad (7c)$$

$$\ell \dot{i} = v_{dc} m - Z i - v, \quad (7d)$$

$$c \dot{v} = i - Y v - i_g, \quad (7e)$$

$$\ell_g \dot{i}_g = v - Z_g i_g - v_b, \quad (7f)$$

here $m = \mu_r \psi(\theta)$, $Z := rI - \ell \omega_0 J$ denotes the filter impedance matrix with $J := \begin{pmatrix} 0 & 1 \\ -1 & 0 \end{pmatrix}$, $Y := gI - c \omega_0 J$ is the shunt admittance matrix, $Z_g := r_g I - \ell_g \omega_0 J$ is the grid impedance matrix, and $v_b := (v_r, 0)$.

For notational convenience we respectively define the net dc current and power transferred to the converter ac-side as $i_{net} := m^\top i$ and $p_{net} := v_{dc} i_{net}$. The ac active and reactive power injections at the switching node, the filter capacitance, and IB nodes in Figure 1 are respectively defined by $p_s := i^\top v_s$ with $v_s := v_{dc} m$, $q_s := i^\top J v_s$, $p_f := i^\top v$, $q_f := i^\top J v$ and $p_g := i_g^\top v_b$, $q_g := i_g^\top J v_b$ [29, Sec. 4.6]. Last, note that the RHS of (7) is continuously differentiable in \mathbb{X} and the main nonlinearity aside (7a) is represented by the modulated terms in (7c) and (7d) with their power-preserving structure (assuming lossless dc-ac conversion) i.e., $p_{net} = p_s$ [17]. We close this section with three remarks on \mathbb{M} and the HAC.

Remark 1 (Möbius strip)

The angle term in (5) is 4π -periodic and thus multi-valued on \mathbb{S}^1 . Hence, we study the evolution of angle trajectories in \mathbb{M} . One representation of \mathbb{M} is the compact boundary of Möbius strip parametrized in \mathbb{R}^3 by $\sigma(w, \varphi)$ with coordinates

$$\sigma_1(w, \varphi) := (\rho - w \cos(\varphi/2)) \cos \varphi,$$

$$\sigma_2(w, \varphi) := (\rho - w \cos(\varphi/2)) \sin \varphi,$$

$$\sigma_3(w, \varphi) := w \sin(\varphi/2),$$

where $\rho \in \mathbb{R}_{> 0}$ is the middle circle radius, w denotes the half-width with $|w| \leq 1/2$, and $\varphi \in \mathbb{S}^1$. Figure 2 illustrates a parametrization of $\sigma(w, \varphi)$ such that $|\partial \sigma(w, \varphi)| = 4\pi$ where $\partial \sigma(w, \varphi)$ denotes the boundary of möbius strip.

Remark 2 (HAC synthesis and properties)

The HAC (5) is inspired by direct angle control [17], and blending the dc and ac dynamics in a grid-forming control design [2, Rem. 2]. The angle feedback in (5) is an odd function and injects angle damping, i.e., it provides dissipation for the angle in (7) in contrast to other control approaches, where the angle variable acts as a mere integrator. HAC offers two degrees of freedom (η and γ) for optimal frequency tuning. Section V presents a practical implementation of HAC. The ratio of control gains η and γ not only trades off the HAC dependency on dc or ac dynamics, but also influences its power-frequency droop slope (see Proposition 7) and transient performance; see Subsection VI-C for a numerical example.

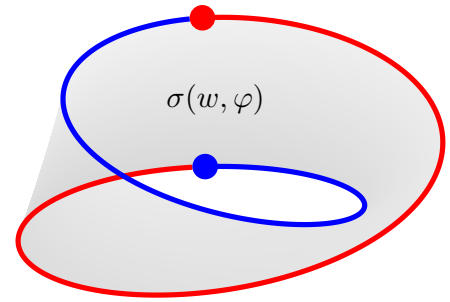


Fig. 2: The boundary of the Möbius strip represents the angle space of (7). The arcs contained in the boundary segments colored in blue and red respectively represent the angles in $[-2\pi, 0]$ and $[0, 2\pi]$.

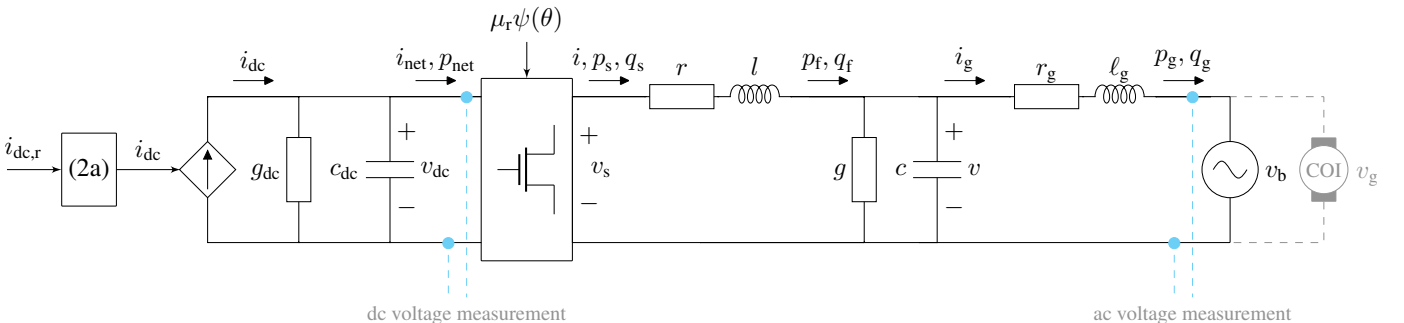


Fig. 1: Schematic of the closed-loop system (7); see Figure 5 for the control diagram defining $i_{dc,r}$ and $\mu_r \psi(\theta)$, and the Section IV-A for the description of the closed-loop system with the COI grid model.

Remark 3 (HAC variants)

It is noteworthy that with particular parameter choices in (5), HAC recover several grid-forming controls. For instance, choosing $\eta = 0$ in (5) leads to a pure angle feedback control i.e., $\omega_c = \omega_0 - \gamma \sin((\theta - \theta_r)/2)$ reminiscent of the droop control [2, Sec. III-C] [10]. Indeed, the droop control is described by $\omega_c := \omega_0 + d_{p-\omega}(p_r - p)$, with the droop gain $d_{p-\omega} \in \mathbb{R}_{>0}$ (see Proposition 7 for a definition), power reference p_r , and $p := i_g^\top v$ being the measured power that (with the assumptions in [10]) is proportional to $\sin(\theta)$. Likewise, HAC relates to dVOC, since around the equilibrium dVOC dynamics (in polar coordinates) reduces to a form that resembles droop control [22], [31]. Further, the dc term with $\eta = \omega_0/v_{dc,r}$ recovers the standard matching control [16] combined with the angle term i.e., $\omega_c = \eta v_{dc} - \gamma \sin((\theta - \theta_r)/2)$. Last, if $\eta \neq \omega_0/v_{dc,r}$ the dc term in (5) is identical to the matching variant in [15].

III. CLOSED-LOOP ANALYSIS

In what follows, we analyze the closed-loop system (7) and provide suitable parametric conditions for the existence, uniqueness, and global stability of the closed-loop equilibria.

A. Existence of Equilibria

Provided that the dc voltage meets its reference in steady state, we will establish that the closed-loop system (7) admits a unique equilibrium set containing two disjoint equilibria

$$\Omega^* := \{x_s^* := (\theta_1^*, y^*), x_u^* := (\theta_2^*, y^*)\}, \quad (9)$$

where $\theta_1^* := \theta_r$, $\theta_2^* := \theta_r + 2\pi$, and $y^* := (i_{dc}^*, v_{dc}^*, i^*, v^*, i_g^*)$ is the unique equilibrium of the states evolving in \mathbb{R}^8 .

Theorem 1 (Existence of equilibria)

The closed-loop system (7) admits two equilibria if there exist a consistent reference $i_r = i_{dc}^*$ in (7b) such that $v_{dc}^* = v_{dc,r}$. These disjoint equilibria only differ by their equilibrium angles being equal to θ_r or $\theta_r + 2\pi$, i.e., they are of the form (9).

Proof. We begin by setting the RHS of (7) to zero

$$\eta(v_{dc}^* - v_{dc,r}) - \gamma \sin((\theta^* - \theta_r)/2) = 0, \quad (10a)$$

$$i_r - \kappa(v_{dc}^* - v_{dc,r}) - i_{dc}^* = 0, \quad (10b)$$

$$i_{dc}^* - g_{dc}v_{dc}^* - m(\theta^*)^\top i^* = 0, \quad (10c)$$

$$v_{dc}^* m(\theta^*) - Z i^* - v^* = 0_2, \quad (10d)$$

$$i^* - Y v^* - i_g^* = 0_2, \quad (10e)$$

$$v^* - Z_g i_g^* - v_b = 0_2. \quad (10f)$$

If the condition of the theorem is met and thus $v_{dc}^* = v_{dc,r}$, (10b) implies that $i_{dc}^* = i_r$ and (10a) reduces to $\gamma \sin((\theta^* - \theta_r)/2) = 0$. Hence the angle equilibria are

$$\theta_1^* = \theta_r \quad \text{and} \quad \theta_2^* = \theta_r + 2\pi. \quad (11)$$

It remains to show (10d)-(10f) admits a unique solution. Rearrange (10d)-(10f) to $A(i^*, v^*, i_g^*) = b$ with

$$A := \begin{pmatrix} -Z & -I & 0_{2 \times 2} \\ I & -Y & -I \\ 0_{2 \times 2} & I & -Z_g \end{pmatrix}$$

and $b := (-v_{dc}^* m(\theta^*), 0_2, v_b)$. It can be easily computed that symmetric part of A , that is, $(1/2)(A + A^\top) \prec 0$. Hence, A^{-1} exists and $(i^*, v^*, i_g^*) := A^{-1}b$ is unique. ■

Remark 4 (Equilibria and the existence condition)

The following comments are in order:

First, Theorem 1 identifies two equilibria in (9) conditioned on a consistent reference i_r inducing $v^* = v_{dc,r}$. This condition can be enforced through appropriate feedforward control or feedback proportional-integral regulation, and it can be entirely omitted if $\eta = 0$ in (5).

Second, the condition is actually not restrictive. In fact, in the next section we will prove that the closed-loop system (7) is AGAS w.r.t. x_s^* under a mild parametric condition. Thus, if x_s^* exists then no other relevant (i.e., stable) equilibria co-exist.

Third, in case the set-points are inconsistent or if the system is subject to exogenous disturbances, then the closed-loop (7) will undergo a so-called droop behavior similar to other grid-forming controls (e.g., [16, Prop. 5] [20, Prop. 4]), i.e., a power imbalance will result in a frequency deviation; see Section V-B for details.

Last, next to x_s^* being AGAS on $\mathbb{M} \times \mathbb{R}^8$, we will establish instability of x_u^* . In fact, when viewing the angle state not as element of \mathbb{M} but more conventionally evolving on \mathbb{S}^1 (i.e., picture projecting Figure 2 downwards to a circle), then the two equilibria $\{x_s^*, x_u^*\}$ represent an identical point on \mathbb{S}^1 . Thus, by working on \mathbb{M} rather than \mathbb{S}^1 we by-passed the topological obstruction to continuous stabilization on \mathbb{S}^1 [28].

B. Stability Analysis

In the sequel, we establish the AGAS of the closed-loop system (7) w.r.t. the equilibrium x_s^* characterized in Theorem 1. This finding relies on the basis of intermediate results, namely, 1) global convergence of the trajectories to Ω^* in (9), 2) local asymptotic stability of x_s^* , and 3) instability of x_u^* . We begin by restating the definition of AGAS [20, Def. 5].

Definition 1 (AGAS)

An equilibrium of a dynamical system is almost globally asymptotically stable if it is asymptotically stable and for all initial conditions, except those contained in a Lebesgue zero-measure set, the trajectories converge to that equilibrium.

Theorem 2 below demonstrates the global attractivity of the equilibria (9) under a mild parametric condition. We want to highlight the innovative bounding scheme of the trigonometric error term $\psi(\theta) - \psi(\theta^*)$ in the proof of Theorem 2, which is novel to our knowledge, and results in less restrictive parametric condition relative to the literature; see Remark 5.

Theorem 2 (Global attractivity)

Consider the closed-loop system (7) and the equilibria Ω^* characterized in Theorem 1. If the system parameters satisfy

$$\frac{\eta}{g_{dc}} + \frac{\eta(\mu_r \|i^*\|)^2}{g_{dc}} + \frac{\eta(\mu_r v_{dc}^*)^2}{r} < \gamma, \quad (12)$$

then all trajectories of (7) globally converge to Ω^* .

Proof. Define the error coordinates $\tilde{x} = (\tilde{\theta}, \tilde{i}_{dc}, \tilde{v}_{dc}, \tilde{i}, \tilde{v}, \tilde{i}_g)$ w.r.t. x_s^* – with the equilibrium angle θ_1^* – in (9) as

$$\tilde{x} := (\theta - \theta_1^*, i_{dc} - i_{dc}^*, v_{dc} - v_{dc}^*, i - i^*, v - v^*, i_g - i_g^*). \quad (13)$$

The error dynamics associated with (7) are described by

$$\dot{\tilde{\theta}} = \eta \tilde{v}_{dc} - \gamma \sin(\tilde{\theta}/2), \quad (14a)$$

$$\tau_{dc} \dot{\tilde{i}}_{dc} = -\kappa \tilde{v}_{dc} - \tilde{i}_{dc}, \quad (14b)$$

$$c_{dc} \dot{\tilde{v}}_{dc} = \tilde{i}_{dc} - g_{dc} \tilde{v}_{dc} - \mu_r e_{\psi}^T i^* - m(\theta)^T \tilde{i}, \quad (14c)$$

$$\ell \dot{\tilde{i}} = m(\theta) \tilde{v}_{dc} + \mu_r e_{\psi} v_{dc}^* - Z \tilde{i} - \tilde{v}, \quad (14d)$$

$$c \dot{\tilde{v}} = \tilde{i} - Y \tilde{v} - \tilde{i}_g, \quad (14e)$$

$$\ell_g \dot{\tilde{i}} = \tilde{v} - Z_g \tilde{i}_g, \quad (14f)$$

where $e_{\psi} := \psi(\theta) - \psi(\theta_1^*)$. Let $\tilde{y} := (\tilde{i}_{dc}, \tilde{v}_{dc}, \tilde{i}, \tilde{v}, \tilde{i}_g)$ and consider the composite parametric LaSalle/Lyapunov function

$$\mathcal{V}(\tilde{x}) := \mathcal{H}(\tilde{y}) + \lambda \mathcal{S}(\tilde{\theta}) = \frac{1}{2} (\tilde{y}^T P \tilde{y}) + 2\lambda \left(1 - \cos \frac{\tilde{\theta}}{2}\right) \quad (15)$$

where $P := \text{blkdiag}(\tau_{dc}/\kappa, c_{dc}, \ell I, cI, \ell_g I)$, $\lambda \in \mathbb{R}_{>0}$, and $\mathcal{V}(\tilde{x}) > 0$ for all $\tilde{x} \neq 0_g$. See Figure 3 for an illustration of $\mathcal{V}(\tilde{x})$. Evaluating $\dot{\mathcal{V}}(\tilde{x})$ along trajectories of (14) yields

$$\begin{aligned} \dot{\mathcal{V}}(\tilde{x}) = & -g_{dc} \tilde{v}_{dc}^2 - \frac{1}{\kappa} \tilde{i}_{dc}^2 - r \|\tilde{i}\|^2 - g \|\tilde{v}\|^2 - r_g \|\tilde{i}_g\|^2 \\ & + \lambda \eta \tilde{v}_{dc} \sin(\tilde{\theta}/2) - \lambda \gamma \sin^2(\tilde{\theta}/2) \\ & - \mu_r \tilde{v}_{dc} e_{\psi}^T i^* + \mu_r v_{dc}^* \tilde{i}^T e_{\psi}, \end{aligned} \quad (16)$$

where we exploited the skew symmetry of J in Z , Y , and Z_g i.e., $\tilde{i}^T (\ell \omega_0 J) \tilde{i} = \tilde{v}^T (c \omega_0 J) \tilde{v} = \tilde{i}_g^T (\ell_g \omega_0 J) \tilde{i}_g = 0$. We apply the identity (66) to the terms in (16) that depend on e_{ψ} :

$$-\mu_r \tilde{v}_{dc} e_{\psi}^T i^* \leq (\epsilon_1 \mu_r \|i^*\|)^2 \tilde{v}_{dc}^2 + \frac{1}{4\epsilon_1^2} \|e_{\psi}\|^2, \quad (17a)$$

$$\mu_r v_{dc}^* \tilde{i}^T e_{\psi} \leq \epsilon_2^2 \|\tilde{i}\|^2 + \frac{(\mu_r v_{dc}^*)^2}{4\epsilon_2^2} \|e_{\psi}\|^2. \quad (17b)$$

with $\epsilon_1, \epsilon_2 \in \mathbb{R}_{>0}$. Next, by applying identities (67) and (70), $\|e_{\psi}\|^2$ is expressed in terms of $\sin(\tilde{\theta}/2)$:

$$\begin{aligned} \|e_{\psi}\|^2 &= (\cos(\theta) - \cos(\theta_1^*))^2 + (\sin(\theta) - \sin(\theta_1^*))^2 \\ &= 2(1 - \cos(\theta) \cos(\theta_1^*) - \sin(\theta) \sin(\theta_1^*)) \\ &= 2(1 - \cos(\theta - \theta_1^*)) = 2(1 - \cos(\tilde{\theta})) = 4 \sin^2(\tilde{\theta}/2). \end{aligned}$$

Replace $\|e_{\psi}\|^2$ by $4 \sin^2(\tilde{\theta}/2)$ in (17), then $\dot{\mathcal{V}}(\tilde{x})$ in (16) is upper-bounded by

$$\begin{aligned} \dot{\mathcal{V}}(\tilde{x}) \leq & \lambda \eta \tilde{v}_{dc} \sin(\tilde{\theta}/2) - \left(\lambda \gamma - \frac{1}{\epsilon_1^2} - \frac{(\mu_r v_{dc}^*)^2}{\epsilon_2^2} \right) \sin^2(\tilde{\theta}/2) \\ & - \left(g_{dc} - (\epsilon_1 \mu_r \|i^*\|)^2 \right) \tilde{v}_{dc}^2 - (r - \epsilon_2^2) \|\tilde{i}\|^2 \\ & - \frac{1}{\kappa} \tilde{i}_{dc}^2 - g \|\tilde{v}\|^2 - r_g \|\tilde{i}_g\|^2 = -\tilde{\zeta}^T Q \tilde{\zeta}, \end{aligned} \quad (18)$$

where $\tilde{\zeta} := (\sin(\tilde{\theta}/2), \tilde{y})$ and $Q := \begin{pmatrix} Q_{11} & 0_{3 \times 6} \\ 0_{6 \times 3} & Q_{22} \end{pmatrix}$ with $Q_{11} :=$

$$\begin{pmatrix} \gamma \lambda - \frac{1}{\epsilon_1^2} - \frac{(\mu_r v_{dc}^*)^2}{\epsilon_2^2} & 0 & -\frac{\eta \lambda}{2} \\ 0 & \frac{1}{\kappa} & 0 \\ -\frac{\eta \lambda}{2} & 0 & g_{dc} - (\epsilon_1 \mu_r \|i^*\|)^2 \end{pmatrix} \quad (19)$$

and $Q_{22} := \text{blkdiag}((r - \epsilon_2^2) I, gI, r_g I)$. By standard Schur complement analysis, $Q \succ 0$ iff

$$\epsilon_1^2 < \frac{g_{dc}}{(\mu_r \|i^*\|)^2} := \alpha \quad \text{and} \quad \epsilon_2^2 < r, \quad (20a)$$

$$\left(\frac{\lambda \eta}{2\sqrt{g_{dc}}} \right)^2 < \left(\gamma \lambda - \frac{1}{\epsilon_1^2} - \frac{(\mu_r v_{dc}^*)^2}{\epsilon_2^2} \right) \left(1 - \frac{\epsilon_1^2}{\alpha} \right). \quad (20b)$$

These bounds can be optimized over the parameters ϵ_1, ϵ_2 , and λ to obtain the least conservative or most compact condition.

To continue assume for now that $\eta > 0$. The simple and favorable choice $\epsilon_1 = \sqrt{\alpha/2}$, $\epsilon_2 = \sqrt{r/2}$, and $\lambda = 2/\eta$ yields that conditions (20) are satisfied and $Q \succ 0$ iff the bound (12) is met. Accordingly, $\dot{\mathcal{V}}(\tilde{x}) < 0$ for all $\tilde{\zeta} \neq 0_g$. For $\eta = 0$, the off-diagonal elements of Q_{11} in (19) vanish. With the same choice of $\epsilon_1 = \sqrt{\alpha/2}$ and $\epsilon_2 = \sqrt{r/2}$, condition (20b) reduces to

$$\frac{2(\mu_r \|i^*\|)^2}{\lambda g_{dc}} + \frac{2(\mu_r v_{dc}^*)^2}{\lambda r} < \gamma. \quad (21)$$

For any $\gamma > 0$, (21) is met by a sufficiently large $\lambda > 0$, which is consistent with condition (12) for $\eta = 0$.

Recall the boundedness of $\tilde{\theta}$ in \mathbb{M} and radial unboundedness of $\mathcal{H}(\tilde{y})$. Since $\dot{\mathcal{V}}(\tilde{x}) \leq 0$, for any $\tilde{x}(0) \in \mathbb{X}$, the set $\mathcal{L}_{\mathcal{V}(\tilde{x}(0))} = \{\tilde{x} \in \mathbb{X} : \mathcal{V}(\tilde{x}) \leq \mathcal{V}(\tilde{x}(0))\}$ is compact and forward invariant. Thus, by LaSalle's invariance principle [32, Th. 4.4], all trajectories of (14) converge to the largest invariant set in $\Omega = \{\tilde{x} \in \mathbb{X} : \dot{\mathcal{V}}(\tilde{x}) = 0\}$. Since $Q \succ 0$, $\mathcal{V}(\tilde{x}) = 0$ iff $\tilde{\zeta} = 0_g$ which holds iff $\sin(\tilde{\theta}/2) = 0$ and $\tilde{y} = 0_g$ that means either $\tilde{\theta} = 0$ or $\tilde{\theta} = 2\pi$ in Ω proving that $\Omega = \Omega^*$. ■

Remark 5 (Feasibility, interpretation, and significance)

Following comments are in order:

First, condition (12) is met for sufficiently large $\gamma > 0$ and it is possible to arbitrarily scale the left-hand side (LHS) terms via $\eta \geq 0$. Condition (12) implies that for small g_{dc} and r , a large ratio γ/η is required. Also, for high $\|i^\|$, v_{dc}^* , and μ_r , the ratio γ/η must be increased. Finally, for pure angle feedback, i.e., $\eta = 0$ and $\gamma > 0$ in (5), condition (12) is always met regardless of the system equilibria and parameters.*

Second, condition (12) is significant because it does not demand a minimum physical damping unlike the conditions in [16], [17], [25], [26], e.g., see the $1/r$ proportionality in (12) or [16, Th. 3]. In practice, this is met by considering a virtual impedance [33] and / or a high-gain current control [34]. In contrast, HAC only needs large enough ratio of gains γ/η to ensure stability. An interpretation is that with large enough angle damping, the inherent converter passivity is sufficient to stabilize the Euclidean states [16].

Third, condition (12) does not depend on the dc source time constant τ_{dc} and control gain κ . Thus, (12) also unveils the robustness of HAC w.r.t. delays in source actuation that suggests the compatibility of HAC with different energy sources on distinct timescales. Furthermore, κ can still be freely chosen to optimize the dc voltage performance.

Last, although HAC dominantly relies on ac dynamics (by recommendation for large γ/η), stabilization does not require the conventional timescale separation of angle, dc, and ac dynamics [35].

Proposition 1 below reveals the local asymptotic stability of the equilibrium x_s^* in (9) under the condition (12).

Proposition 1 (Local asymptotic stability)

Consider the closed-loop system (7) and assume that condition (12) holds. Then the equilibrium x_s^* in (9) is locally asymptotically stable.

Proof. Consider the error dynamics (14) and the Lyapunov function (15) that satisfies $\mathcal{V}(0_g) = 0$ and $\mathcal{V}(\tilde{x}) > 0$ for all $\tilde{x} \neq 0_g$. Furthermore, if (12) holds, $\dot{\mathcal{V}}(\tilde{x}) < 0$ for all $\tilde{x} \neq 0_g$ in a sufficiently small neighborhood of the origin. Consider a c -sublevel set of $\mathcal{V}(\tilde{x})$ i.e., $\mathcal{L}_c := \{\tilde{x} \in \mathbb{X} : \mathcal{V}(\tilde{x}) \leq c, c \in \mathbb{R}_{>0}\}$, which is forward invariant under the flow (7) since $\dot{\mathcal{V}}(\tilde{x}) \leq 0$. Take c to be sufficiently small such that the origin is the only equilibrium in \mathcal{L}_c (recall that the equilibria in (9) are disjoint). Thus, by Lyapunov's direct method [32, Th. 3.1] the origin is a locally asymptotically stable equilibrium of (14). ■

Proposition 2 reveals instability of x_u^* in (9) and characterizes its region of attraction as a Lebesgue zero-measure set.

Proposition 2 (Unstable equilibrium point)

Consider the closed-loop system (7) and assume that condition (12) holds. The equilibrium x_u^* in (9) is unstable and its region of attraction has zero Lebesgue measure.

The proof is provided in Appendix A. Remark 6 reveals the topological peculiarity of the Lyapunov function (15) at x_u^* .

Remark 6 (Saddle point of the Lyapunov function)

The unstable equilibrium $x_u^* = (\theta_2^*, y^*)$ is a min-max saddle point of the Lyapunov function $\mathcal{V}(x - x_s^*) = \mathcal{V}(\theta - \theta_1^*, y - y^*)$ in (15) i.e., it can be shown that

$$\mathcal{V}(\theta - \theta_1^*, 0_8) \leq \mathcal{V}(\theta_2^* - \theta_1^*, 0_8) \leq \mathcal{V}(\theta_2^* - \theta_1^*, y - y^*),$$

for all (θ, y) in an open neighborhood of x_u^* . This is due to the fact that the global minimum of $\mathcal{H}(y - y^*)$ in \mathbb{R}^8 and the maximum of $\mathcal{S}(\theta - \theta_r)$ in \mathbb{M} coincide at x_u^* ; see Figure 3 for an abstract illustration assuming that $y, \theta \in \mathbb{R}$.

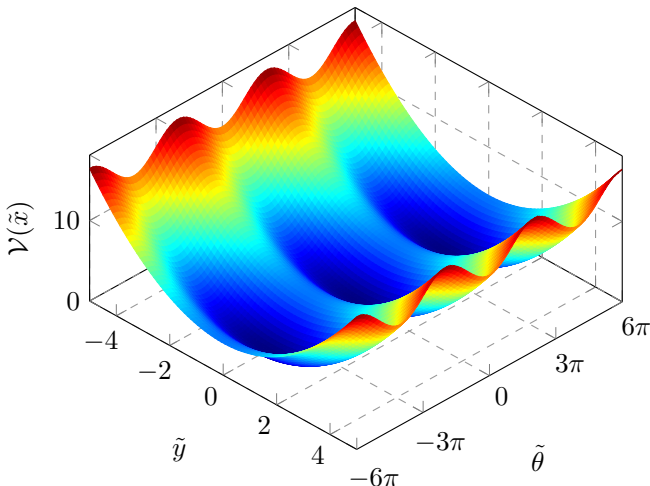


Fig. 3: Illustration of the Lyapunov function (15) under the simplifying assumption that $\tilde{y}, \tilde{\theta} \in \mathbb{R}$, $P = 1$, and $\lambda = 1$.

Having established the intermediate results, Theorem 3 presents our main result i.e., AGAS of system (7) w.r.t. x_s^* .

Theorem 3 (Main result: AGAS)

Consider the closed-loop system (7) and assume condition (12) holds. Then x_s^* in (9) is almost globally asymptotically stable.

IV. DYNAMIC GRID AND CURRENT-LIMITING CONTROL

In this section, we construct two extensions on the basis of the robust results in Section III. First, we consider the connection of the converter to a dynamic grid represented by an COI model and investigate closed-loop stability. Second, we account for the converter current constraint and design a novel current-limiting control that is compatible with HAC.

A. Modeling the Connection of Converter and Dynamic Grid

Under the slow coherency assumptions [36, Chap. 2] [37], an interconnected network of SGs can be represented with an equivalent COI model that relies on the aggregation of swing dynamics [38, Sec. 6.10] [39, Sec. 3.2]. The angle and frequency dynamics of the COI grid model are described by

$$\dot{\theta}_g = \omega, \quad (22a)$$

$$J\dot{\omega} = T_m - D\omega - T_e, \quad (22b)$$

where $J \in \mathbb{R}_{>0}$ is the moment of inertia and it is defined (in terms of the base power $S_{r,g}$ and the inertia constant H) by $J := 2HS_{r,g}/\omega_0^2$ [40, Eq. 5.10]. Moreover, $T_m \in \mathbb{R}$ denotes the mechanical torque, $D \in \mathbb{R}_{>0}$ denotes the aggregated damping and droop coefficient that models the aggregated governor action, and $T_e \in \mathbb{R}$ is the electrical torque. Considering the structural similarity of (22) and the full SG dynamics [25], we define the dynamic grid voltage as

$$v_{g,abc} := b\omega(\sin \theta_g, \sin(\theta_g - 2\pi/3), \sin(\theta_g + 2\pi/3)), \quad (23)$$

where $b \in \mathbb{R}_{>0}$ is constant [25, Eq. 9]. Thus, T_e in (22b) can be written in terms of grid voltage and current as [25, Eq. 10]

$$T_e = \omega^{-1} i_{g,abc}^\top v_{g,abc}. \quad (24)$$

Note that if $J \rightarrow \infty$ and b is chosen such that $\|v_g\| \rightarrow v_r$ as $\omega \rightarrow \omega_0$, (22)-(24) recovers the IB grid model with constant frequency and voltage magnitude (see Section II-B).

Consider a converter controlled by HAC and connected to the COI grid model via an inductive line; see Figure 1. Combining (2), (3), (5), and (22)-(24) the overall closed-loop dynamics in a dq-frame aligned with θ_g is

$$\dot{\theta} = \omega_0 + \eta(v_{dc} - v_{dc,r}) - \gamma \sin((\theta - \theta_r)/2) - \omega, \quad (25a)$$

$$\tau_{dc} \dot{i}_{dc} = i_r - \kappa(v_{dc} - v_{dc,r}) - i_{dc}, \quad (25b)$$

$$c_{dc} \dot{v}_{dc} = i_{dc} - g_{dc} v_{dc} - m^\top i, \quad (25c)$$

$$\ell \dot{i} = v_{dc} m - Z(\omega) i - v, \quad (25d)$$

$$c \dot{v} = i - Y(\omega) v - i_g, \quad (25e)$$

$$\ell_g \dot{i}_g = v - Z_g(\omega) i_g - b\omega e_1, \quad (25f)$$

$$J \dot{\omega} = T_m - D\omega + b e_1^\top i_g, \quad (25g)$$

where $\theta := \theta_c - \theta_g$ denotes the converter relative angle w.r.t. the COI and $e_1 := (1, 0)$. Note the impedance and admittance matrices in (25d)-(25f) are frequency-dependent (cf. to constant matrices in (7d)-(7f)).

B. Equilibria Characterization and Closed-Loop Stability

To begin with, define the augmented closed-loop state vector

$$\underline{x} := (\theta, i_{dc}, v_{dc}, \omega, i, v, i_g) \in \underline{\mathbb{X}} := \mathbb{M} \times \mathbb{R}^9. \quad (26)$$

Assume that the reference dc current and mechanical torque in (25b) and (25g) are set such that the equilibrium dc voltage and frequency coincide with $v_{dc,r}$ and ω_0 . Following the same procedure as in the proof Theorem 1, dynamical system (25) admits two equilibria with the same structure as Ω^* in (9) i.e.,

$$\underline{\Omega}^* := \{ \underline{x}_s^* := (\theta_1^*, \underline{y}^*), \underline{x}_u^* := (\theta_2^*, \underline{y}^*) \}, \quad (27)$$

with $\theta_1^* := \theta_r$, $\theta_2^* := \theta_r + 2\pi$, and $\underline{y}^* := (i_{dc}^*, v_{dc}^*, \omega^*, i^*, v^*, i_g^*)$ denoting the unique equilibrium associated with states evolving in \mathbb{R}^9 . Theorem 4 delivers the same result as Theorem 2 i.e., global stability of $\underline{\Omega}^*$ under the flow defined by (25).

Theorem 4 (Global stability with dynamic grid model)

Consider the closed-loop system (25) and the equilibria $\underline{\Omega}^*$ defined in (27). If the system and control parameters satisfy

$$D > D_{\min} := \frac{(\ell \|i^*\|)^2}{r} + \frac{(c \|v^*\|)^2}{g} + \frac{(\ell_g \|i_g^*\|)^2}{r_g}, \quad (28a)$$

$$\gamma > \frac{\eta}{g_{dc}} + \frac{\eta(\mu_r \|i^*\|)^2}{g_{dc}} + \frac{\eta(\mu_r v_{dc}^*)^2}{r} + \frac{1}{2(D - D_{\min})}, \quad (28b)$$

then all trajectories of (25) globally converge to $\underline{\Omega}^*$.

Proof. Define the error coordinates as $\tilde{x} := \underline{x} - \underline{x}_s^*$. The error dynamics associated with (25) are described by

$$\begin{aligned} \dot{\tilde{\theta}} &= \eta \tilde{v}_{dc} - \gamma \sin(\tilde{\theta}/2) - \tilde{\omega}, \\ \tau_{dc} \dot{\tilde{i}}_{dc} &= -\kappa \tilde{v}_{dc} - \tilde{i}_{dc}, \\ c_{dc} \dot{\tilde{v}}_{dc} &= \tilde{i}_{dc} - g_{dc} \tilde{v}_{dc} - \mu_r e_{\psi}^\top i^* - m(\theta)^\top \tilde{i} \\ \dot{\tilde{i}} &= \tilde{v}_{dc} m(\tilde{\theta}) + \mu_r v_{dc}^* e_{\psi} - r \tilde{i} - \ell \omega \tilde{J} \tilde{i} - \ell \tilde{\omega} \tilde{J} i^* - \tilde{v}, \\ c \dot{\tilde{v}} &= \tilde{i} - g \tilde{v} - c \omega \tilde{J} \tilde{v} - c \tilde{\omega} \tilde{J} v^* - \tilde{i}_g, \\ \ell_g \dot{\tilde{i}}_g &= \tilde{v} - r_g \tilde{i}_g - \ell_g \omega \tilde{J} \tilde{i}_g - \ell_g \tilde{\omega} \tilde{J} i_g^* - b e_1 \tilde{\omega}, \\ \tilde{J} \dot{\tilde{\omega}} &= -D \tilde{\omega} + b e_1^\top \tilde{i}_g. \end{aligned}$$

where $e_{\psi} := \psi(\theta) - \psi(\theta_1^*)$. Define $\tilde{y} := (\tilde{i}_{dc}, \tilde{v}_{dc}, \tilde{\omega}, \tilde{i}, \tilde{v}, \tilde{i}_g) \in \mathbb{R}^9$, and consider the following Lyapunov function

$$\underline{\mathcal{V}}(\tilde{x}) := \frac{1}{2} (\tilde{y}^\top \underline{P} \tilde{y}) + 2\lambda \left(1 - \cos \frac{\tilde{\theta}}{2} \right)$$

where $\underline{P} := \text{blkdiag}(\tau_{dc}/\kappa, c_{dc}, J, \ell I, cI, \ell_g I)$ and $\lambda \in \mathbb{R}_{>0}$. Evaluating $\dot{\underline{\mathcal{V}}}(\tilde{x})$ along the error trajectories yields

$$\begin{aligned} \dot{\underline{\mathcal{V}}}(\tilde{x}) &= -\frac{1}{\kappa} \tilde{i}_{dc}^2 - g_{dc} \tilde{v}_{dc}^2 - D \tilde{\omega}^2 - r \|\tilde{i}\|^2 - g \|\tilde{v}\|^2 - r_g \|\tilde{i}_g\|^2 \\ &\quad - \lambda \gamma \sin^2(\tilde{\theta}/2) + \lambda \eta \tilde{v}_{dc} \sin(\tilde{\theta}/2) + \lambda \tilde{\omega} \sin(\tilde{\theta}/2) \\ &\quad - \tilde{i}^\top (\ell \tilde{J} i^*) \tilde{\omega} - \tilde{v}^\top (c \tilde{J} v^*) \tilde{\omega} - \tilde{i}_g^\top (\ell_g \tilde{J} i_g^*) \tilde{\omega} \\ &\quad - \mu_r e_{\psi}^\top i^* \tilde{v}_{dc} + \mu_r v_{dc}^* \tilde{i}^\top e_{\psi}. \end{aligned} \quad (30)$$

From the proof of Theorem 2 recall that $\|e_{\psi}\|^2 = 4 \sin^2(\tilde{\theta}/2)$ and apply (66) to the cross-terms in (30) that depend on v_{dc}^* , i^* , v^* , and i_g^* . Then $\dot{\underline{\mathcal{V}}}(\tilde{x})$ is upper-bounded by

$$\begin{aligned} \dot{\underline{\mathcal{V}}}(\tilde{x}) &\leq -\frac{1}{\kappa} \tilde{i}_{dc}^2 - \left(g_{dc} - (\epsilon_1 \mu_r \|i^*\|)^2 \right) \tilde{v}_{dc}^2 - (D - \underline{\alpha}) \tilde{\omega}^2 \\ &\quad - (r - \epsilon_2^2 - \epsilon_3^2) \|\tilde{i}\|^2 - (g - \epsilon_4^2) \|\tilde{v}\|^2 - (r_g - \epsilon_5^2) \|\tilde{i}_g\|^2 \\ &\quad - \left(\gamma \lambda - \frac{1}{\epsilon_1^2} - \frac{(\mu_r v_{dc}^*)^2}{\epsilon_2^2} \right) \sin^2(\tilde{\theta}/2) \\ &\quad - \lambda \tilde{\omega} \sin(\tilde{\theta}/2) + \lambda \eta \tilde{v}_{dc} \sin(\tilde{\theta}/2) \end{aligned} \quad (31)$$

where $\epsilon_j \in \mathbb{R}_{>0}$ for $j = 1, \dots, 5$ and

$$\underline{\alpha} := \left(\frac{\ell \|i^*\|}{2\epsilon_3} \right)^2 + \left(\frac{c \|v^*\|}{2\epsilon_4} \right)^2 + \left(\frac{\ell_g \|i_g^*\|}{2\epsilon_5} \right)^2.$$

Defining $\underline{\zeta} := (\sin(\tilde{\theta}/2), \tilde{y})$ the bound in (31) takes the quadratic form i.e., $\dot{\underline{\mathcal{V}}}(\tilde{x}) \leq -\underline{\zeta}^\top \underline{Q} \underline{\zeta}$, where $\underline{Q} = \text{blkdiag}(\underline{Q}_{11}, \underline{Q}_{22})$ with $\underline{Q}_{11} :=$

$$\begin{pmatrix} \gamma \lambda - \frac{1}{\epsilon_1^2} - \frac{(\mu_r v_{dc}^*)^2}{\epsilon_2^2} & 0 & -\frac{\eta \lambda}{2} & \frac{\lambda}{2} \\ 0 & \frac{1}{\kappa} & 0 & 0 \\ -\frac{\eta \lambda}{2} & 0 & g_{dc} - (\epsilon_1 \mu_r \|i^*\|)^2 & 0 \\ \frac{\lambda}{2} & 0 & 0 & D - \underline{\alpha} \end{pmatrix},$$

and $\underline{Q}_{22} := \text{blkdiag}((r - \epsilon_2^2 - \epsilon_3^2)I, (g - \epsilon_4^2)I, (r_g - \epsilon_5^2)I)$. Choosing the free parameters as $\lambda = 2/\eta$, $\epsilon_1 = \sqrt{g_{dc}}/(\sqrt{2}\mu_r \|i^*\|)$, $\epsilon_2 = \sqrt{r}/2$, $\epsilon_3 = \sqrt{r}/2$, $\epsilon_4 = \sqrt{g}/2$ and $\epsilon_5 = \sqrt{r_g}/2$ renders $\underline{Q}_{22} \succ 0$. Under this favorable choice of parameters, $\underline{Q}_{11} \succ 0$ if and only if (28) is satisfied. Thus, $\underline{Q} \succ 0$ and $\dot{\underline{\mathcal{V}}}(\tilde{x}) < 0$ for all $\underline{\zeta} \neq 0_{10}$. Following the LaSalle's invariance argument in the proof of Theorem 2, it is straightforward to show that the trajectories of (29) globally converge to the largest invariant set contained in $\underline{\Omega} := \{ \tilde{x} \in \underline{\mathbb{X}} : \dot{\underline{\mathcal{V}}}(\tilde{x}) = 0 \}$ and $\underline{\Omega} = \underline{\Omega}^*$. ■

Remark 7 (Extended stability conditions)

Condition (28a) is met if the COI model is sufficiently damped (see [23], [25], [26] for discussions on the critical damping requirement) and with large enough γ condition (28b) is satisfied (see Remark 5). The conditions in (28) almost decouple into the previous stability condition (cf. (28b) and (12)) and the damping requirement (28a) (that can be perceived as characterization of the grid types to which the converter can be interfaced). For $D \gg D_{\min}$ conditions (28) reduce to (12). An interpretation of the trade-off between γ and D is that with large D the timescale of COI model approaches that of the converter. Thus, synchronization demands less angle damping due to more coherent frequency dynamics.

The proof of Theorem 4 extends the proof of Theorem 2. By following analogous arguments, it is possible to extend Propositions 1 and 2 and Theorem 3 to (25) under condition (28). For brevity of presentation, we omit the straightforward albeit lengthy calculations.

C. Compatible Current-Limiting Control Synthesis

In practice, power converters have tight state constraints for safety: in particular, their filter current magnitude needs to be constrained to a prescribed limit for protecting the semiconductor switches. There are ad hoc current-limiting techniques (without theoretical certificates e.g., see [41]) for *grid-following* converters (see [1] for a definition). The design of current limitation strategies for grid-forming (i.e., voltage source) converters is an active research topic [2], [33], [42], [43]. To this date, a universally satisfactory solution that safeguards the converter against various contingencies (e.g., load-induced over-current and balanced / unbalanced faults) is not known. In what follows, we propose a new current-limiting control and highlight its compatibility with the HAC.

To begin with, by viewing the current dynamics in isolation, we derive the magnitude dynamics associated with (7d) by means of polar coordinates transformation (see Appendix B2 for details). First, expand the current dynamics in (7d):

$$\ell \dot{i}_d = \mu_r v_{dc} \cos(\theta) - r i_d + \ell \omega_0 i_q - v_d, \quad (32a)$$

$$\ell \dot{i}_q = \mu_r v_{dc} \sin(\theta) - r i_q - \ell \omega_0 i_d - v_q. \quad (32b)$$

Consider that $\|i\| = \sqrt{i_d^2 + i_q^2}$ and thus

$$\frac{d}{dt} \|i\|^2 = 2 \|i\| \frac{d}{dt} \|i\| = 2(i_d \dot{i}_d + i_q \dot{i}_q). \quad (33)$$

Replace i_d and i_q with $\|i\| \cos(\theta_i)$ and $\|i\| \sin(\theta_i)$ where $\theta_i := \tan^{-1}(i_q/i_d)$ and multiply (33) with $\ell/2 \|i\|$:

$$\ell \frac{d}{dt} \|i\| = \ell \cos(\theta_i) \dot{i}_d + \ell \sin(\theta_i) \dot{i}_q. \quad (34)$$

Next, substitute v_d and v_q in (32) with $\|v\| \cos(\theta_v)$ and $\|v\| \sin(\theta_v)$ where $\theta_v := \tan^{-1}(v_q/v_d)$. Replacing $\ell \dot{i}_d$ and $\ell \dot{i}_q$ in (34) with the RHS of (32) and exploiting (70) results in

$$\ell \frac{d}{dt} \|i\| = \mu_r v_{dc} \cos(\theta - \theta_i) - r \|i\| - \|v\| \cos(\theta_v - \theta_i). \quad (35)$$

So far μ_r in (35) was assumed to be a positive constant; see the definition of $m_{\alpha\beta}(\mu_r, \theta_c)$ in (2). We now re-parametrize the to-be-controlled modulation magnitude as

$$\mu := (1 - \Delta_\mu) \mu_r, \quad (36)$$

where $\Delta_\mu : \mathbb{X} \rightarrow \mathbb{R}_{(0,1)}$ is a locally Lipschitz function specified later. Replacing μ_r in (35) with (36) results in

$$\ell \frac{d}{dt} \|i\| = \mu_r v_{dc} \cos(\theta - \theta_i) (1 - \mathcal{D} - \Delta_\mu) - r \|i\|, \quad (37)$$

where

$$\mathcal{D} := \frac{\|v\| \cos(\theta_v - \theta_i)}{\mu_r v_{dc} \cos(\theta - \theta_i)} \quad (38)$$

takes value in $\mathbb{R}_{(0,1)}$ under normal operation and can be constructed from current and voltage measurements (the cosines of the angle differences in (38) can be computed with similar techniques as in the Section V).

In the sequel, we treat \mathcal{D} as a fictitious disturbance – capturing the influence of other states – in magnitude dynamics (37). Consider a threshold current $i_{th} \in \mathbb{R}_{>0}$ that $\|i\|$ should not exceed. We aim to design a Δ_μ such that 1) the RHS of (37) is strictly negative for all $\|i\| > i_{th}$ and 2) ideally (i.e., not

necessarily) $\Delta_\mu = 0$ for $\|i\| \leq i_{th}$. The design of Δ_μ in Proposition 3 is inspired by ideas from feedback linearization [32, Chap. 13] and disturbance decoupling techniques. Moreover, our design follows the intuition that for limiting the ac current, the dc power (i.e., p_{net} in Figure 1) must be constrained by controlling the modulation magnitude.

Proposition 3 (Bivariate current-limiting control)

Consider the current magnitude dynamics (37) and assume that $|\theta - \theta_i| < \pi/2$ and $\mathcal{D} \in \mathbb{R}_{(0,1)}$. Define

$$\Delta_\mu := \frac{(1 - \mathcal{D}) e^{\beta(\|i\| - i_{th})}}{1 + (1 - \mathcal{D}) (e^{\beta(\|i\| - i_{th})} - 1)}, \quad (39)$$

with $\beta \in \mathbb{R}_{>0}$, then $\|i\|$ is strictly decreasing for $\|i\| > i_{th}$.

Proof. Define $\mathcal{C} := 1 - \mathcal{D}$ and observe that

$$\lim_{(\|i\|, \mathcal{C}) \rightarrow (i_{th}^+, 0^+)} \Delta_\mu = 0 \quad \text{and} \quad \lim_{(\|i\|, \mathcal{C}) \rightarrow (+\infty, 1^-)} \Delta_\mu = 1.$$

Moreover, Δ_μ is strictly increasing in both $\|i\|$ and \mathcal{C} i.e.,

$$\frac{\partial \Delta_\mu}{\partial \|i\|} = \frac{\beta \mathcal{C} (1 - \mathcal{C}) e^{\beta(\|i\| - i_{th})}}{(1 + \mathcal{C} (e^{\beta(\|i\| - i_{th})} - 1))^2} > 0, \quad (40a)$$

$$\frac{\partial \Delta_\mu}{\partial \mathcal{C}} = \frac{e^{\beta(\|i\| - i_{th})}}{(1 + \mathcal{C} (e^{\beta(\|i\| - i_{th})} - 1))^2} > 0. \quad (40b)$$

Since Δ_μ is strictly monotone and continuous with finite limits, then it is bounded by its left and right limits i.e., $\Delta_\mu \in (0, 1)$ for all $\mathcal{C} \in (0, 1)$ and $\|i\| > i_{th}$. Further, since $\Delta_\mu|_{\|i\|=i_{th}} = \mathcal{C}$ and (40) hold then $\mathcal{C} < \Delta_\mu < 1$ for any \mathcal{C} and $\|i\| > i_{th}$. Thus, by the assumptions on $\theta - \theta_i$, and with Δ_μ as in (39), the RHS of (37) is strictly negative for $\|i\| > i_{th}$. Nagumo's theorem [44, Th. 3.1] yields that $\|i(t)\|$ is strictly decreasing whenever $\|i(t)\| > i_{th}$. ■

Observe that $\Delta_\mu \in \mathbb{R}_{(0,1)}$ is required since μ in (36) has to be positive in practice. Subsequently, the assumption that $\mathcal{D} \in \mathbb{R}_{(0,1)}$ is vital; otherwise, the current magnitude in (37) cannot be bounded by controlling μ via bounded Δ_μ .

Remark 8 (Comments on the current-limiting control)

The following comments are in order:

First, the bivariate function Δ_μ in (39) should be understood as a barrier-type function that reduces μ in (36) and thus the switching voltage magnitude $\|v_s\|$ (see Figure 1) when $\|i\| > i_{th}$; observe the influence of Δ_μ on μ in Figure 4. The maximum reduction of μ occurs as $\mathcal{D} \rightarrow 0$ corresponding to a severe contingency e.g., a fault at the filter capacitance node driving $\|v\| \rightarrow 0$ (see Subsection VI-B for an example).

Second, the parameter β controls the curvature and the exponential decay rate of μ in $\|i\|$. Note that $\Delta_\mu \rightarrow 0$ as $\beta \rightarrow +\infty$ for $\|i\| < i_{th}$ and for any \mathcal{D} , however large β results in an aggressive controller resembling a sign function.

Third, practical implementation of \mathcal{D} in (38) can be prone to measurement imperfections. Therefore, if \mathcal{D} admits a non-zero lower bound i.e., $0 < \mathcal{D}_{min} < \mathcal{D}$, it allows to implement a variant of (39) that is independent of \mathcal{D} . Such disturbance-free implementation of Δ_μ is obtained by replacing \mathcal{D} with \mathcal{D}_{min} in (39). In practice, \mathcal{D}_{min} is chosen by estimating \mathcal{D} for the worst-case scenario.

Last, the result of the Proposition 3 can be improved when augmenting \mathcal{D} with the dissipation term $r\|i\|$ in (37). However, in practice $r\|i\|$ is negligible compared to the denominator of (38) (because of insignificant resistance e.g., see Table I).

The assumptions in Proposition 3 (i.e., bounded angle and disturbance) are standard in small-signal / input-to-state stability and protection design. Moreover, the bound on the disturbance feasible set i.e., $\mathcal{D} \in \mathbb{R}_{(0,1)}$ can actually be extended to $\mathcal{D} \in \mathbb{R}_{(0,2)}$. To make this idea clear for now assume that $\mu = \mu_r$, then multiplying the nominator and denominator (38) with $\|i\|$ gives $\mathcal{D} = p_f/p_s$ (see Figure 1). Thus, $\mathcal{D} > 1$ equals $p_f > p_s$ corresponding to the – less likely – scenario in which converter absorbs power from grid, e.g., after loss of load. In this case, replacing $1 - \mathcal{D}$ with $|1 - \mathcal{D}|$ in (39) (while preserving the local Lipschitz continuity of Δ_μ) guarantees that the RHS of (37) is negative for $\mathcal{D} \in \mathbb{R}_{(0,2)}$.

It remains to be shown that tampering with the current magnitude in (37) does not jeopardize the overall system stability. Proposition 4 gives an affirmative answer: under (12) and with current-limiting control (36) the desired closed-loop equilibrium of (7) remains locally asymptotically stable.

Proposition 4 (HAC and current-limiting control)

Consider the closed-loop system (7) where μ_r is replaced by the bounded μ in (36). Assume that the modified dynamics admits equilibria of the form (9) and condition (12) holds. Then the equilibrium x_s^* is locally asymptotically stable.

Proof. By replicating the proof of Theorem 1 it follows that

$$\begin{aligned} \dot{\mathcal{V}}(\tilde{x}) \leq & - \left(\lambda\gamma - \frac{1}{\epsilon_1^2} - \frac{(\mu v_{dc}^*)^2}{\epsilon_2^2} \right) \sin^2(\tilde{\theta}/2) - \frac{1}{\kappa} \tilde{v}_{dc}^2 \\ & - \left(g_{dc} - (\epsilon_1 \mu \|i^*\|^2) \right) \tilde{v}_{dc}^2 - (r - \epsilon_2^2) \|\tilde{i}\|^2 \\ & - g \|\tilde{v}\|^2 - r_g \|\tilde{i}_g\|^2 + \lambda\eta \tilde{v}_{dc} \sin(\tilde{\theta}/2). \end{aligned} \quad (41)$$

Since $\mu < \mu_r$, the RHS of (41) is smaller than the bound in (18), therefore $\dot{\mathcal{V}}(\tilde{x}) \leq -\tilde{\zeta}^\top Q \tilde{\zeta}$ as in (18). Note that $\mathcal{V}(0_9) =$

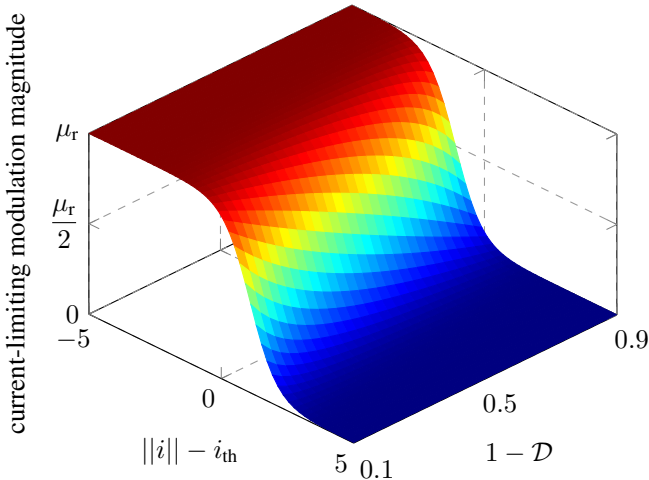


Fig. 4: Illustration of μ in (36) with Δ_μ in (39). For clarity of presentation, here $\beta = 2$ and $\mathcal{D} \in \mathbb{R}_{(0,1,0.9)}$. For small \mathcal{D} (i.e., a severe contingency) Δ_μ initiates the modulation magnitude decay at a lower current compared to a scenario with large \mathcal{D} .

0 , $\mathcal{V}(\tilde{x}) > 0$ for all $\tilde{x} \neq 0_9$. By the proof of Theorem 2 if (12) holds, $\dot{\mathcal{V}}(\tilde{x}) < 0$ for all $\tilde{x} \neq 0_9$ in a sufficiently small neighborhood of the origin. The local asymptotic stability of x_s^* immediately follows from Lyapunov’s direct method [32, Th. 3.1] as in the proof of Proposition 1. ■

It is worth mentioning that the current-limiting control (36) is agnostic to the HAC. Hence, it is expected that (36) is practically compatible with different grid-forming controls in [2] (although possibly without any stability guarantees). The performance of control (36) for a three-phase-to-ground fault scenario is verified in the Subsection VI-B.

V. HAC IMPLEMENTATION AND DROOP BEHAVIOR

In what follows, we describe a practical HAC implementation, introduce a feedforward ac voltage and power control, and unmask the power-frequency droop behavior of HAC.

A. Implementation of HAC and Feedforward Control

The formulation of HAC in (5) relies on the explicit relative angle reference and measurement that are not available in practice. Hence, we seek an alternative implementation based on the dc and ac voltage measurements, and given set-points.

The dc term in (5) is constructed by measuring the dc voltage; see Figure 1. The IB voltage is also measured and transformed to $\alpha\beta$ -frame (see Appendix B2 for details). Subsequently, an implicit IB angle measurement is obtained i.e., $\psi(\theta_b) = v_{b,\alpha\beta} / \|v_{b,\alpha\beta}\|$. Note that $\psi(\theta_c)$ is internally available from the modulation vector m . Thus, by the means of (69) and (70), an implicit relative angle measurement $\psi(\theta)$ is derived

$$\psi(\theta) = (\psi(\theta_c)^\top \psi(\theta_b), \psi(\theta_c)^\top J\psi(\theta_b)). \quad (42)$$

Given a relative angle reference $\psi(\theta_r)$ and measurement (42), Proposition 5 explains the derivation of angle feedback in (5).

Proposition 5 (Angle feedback implementation)

Given $\psi(\theta_r)$ and $\psi(\theta)$ derived by (42), if $|\theta - \theta_r| < \pi$ then

$$\sin\left(\frac{\theta - \theta_r}{2}\right) = \frac{\psi(\theta_r)^\top J\psi(\theta)}{\sqrt{2(1 + \psi(\theta_r)^\top \psi(\theta))}}. \quad (43)$$

Proof. Consider $\psi(\theta_r)^\top J\psi(\theta)$ and apply (69):

$$\begin{aligned} \psi(\theta_r)^\top J\psi(\theta) &= \sin(\theta) \cos(\theta_r) - \sin(\theta_r) \cos(\theta) \\ &= \sin(\tilde{\theta}) = 2 \sin(\tilde{\theta}/2) \cos(\tilde{\theta}/2), \end{aligned}$$

where $\tilde{\theta} := \theta - \theta_r$. Next, consider $\psi(\theta_r)^\top \psi(\theta)$ and apply (70):

$$\psi(\theta_r)^\top \psi(\theta) = \cos(\theta) \cos(\theta_r) + \sin(\theta) \sin(\theta_r) = \cos(\tilde{\theta}).$$

Subsequently, applying identity (68) results in

$$\sqrt{2(1 + \psi(\theta_r)^\top \psi(\theta))} = \sqrt{2(1 + \cos(\tilde{\theta}))} = 2|\cos(\tilde{\theta}/2)|.$$

Hence, the RHS of (43) is equal to

$$\frac{\cos(\tilde{\theta}/2) \sin(\tilde{\theta}/2)}{|\cos(\tilde{\theta}/2)|} = \text{sgn}(\cos(\tilde{\theta}/2)) \sin(\tilde{\theta}/2). \quad (44)$$

Thus, if $|\tilde{\theta}| < \pi$ then $\text{sgn}(\cos(\tilde{\theta}/2)) = 1$ and (43) holds. ■

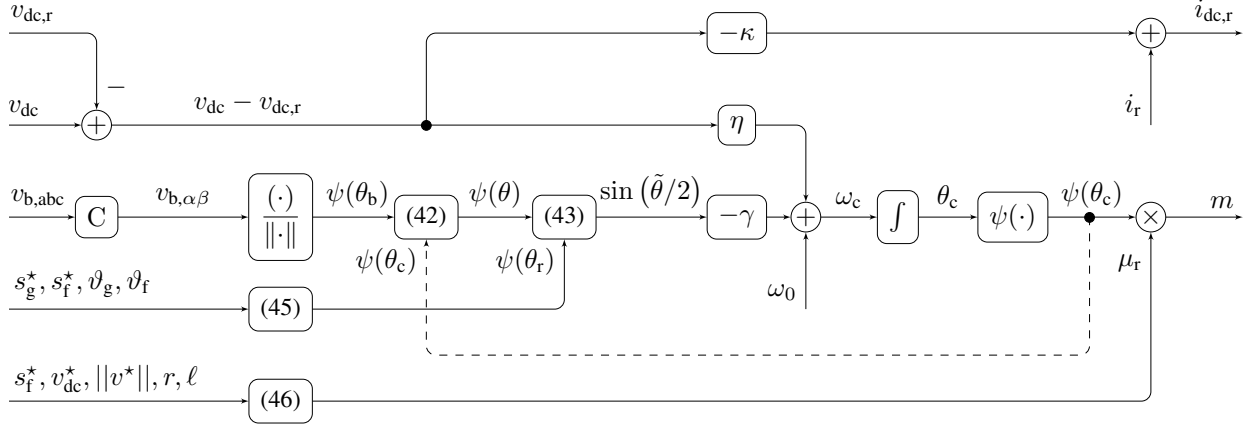


Fig. 5: Block diagram of the feedback controls (3) and (5) with implementation (43), in combination with the feedforward controls (45) and (46) for the closed-system (7).

As well as $\psi(\theta_r)$ in Proposition 5, the reference modulation magnitude μ_r (see Figure 1) is not explicitly available in practice. Rather power references $p_{g,r}$ and $q_{g,r}$ (associated with p_g and q_g in Figure 1) are specified. In what follows, we describe consistent definitions for $\psi(\theta_r)$ and μ_r that rely on the steady-state dc voltage, ac voltage magnitude, and power flows (see (59) and [20, Def. 2] for a definition).

Proposition 6 (Consistent definition of $\psi(\theta_r)$ and μ_r)

Given the voltages v_{dc}^* , $\|v^*\|$, and the references $p_{g,r}$ and $q_{g,r}$ consistent with the equilibrium values i.e., $p_{g,r} = p_g^*$ and $q_{g,r} = q_g^*$, the consistent references are defined by

$$\psi(\theta_r) := \mathbf{R}(\delta)^\top \left(\hat{s}_g^{*\top} \begin{pmatrix} +1 & 0 \\ 0 & -1 \end{pmatrix} \hat{s}_f^*, \hat{s}_g^{*\top} \begin{pmatrix} 0 & +1 \\ +1 & 0 \end{pmatrix} \hat{s}_f^* \right), \quad (45)$$

$$\mu_r := \sqrt{(p_f^{*2} + q_f^{*2})(r^2 + (\ell\omega_0)^2)} / v_{dc}^* \|v^*\|, \quad (46)$$

with $\delta := \tan^{-1}(\ell_g\omega_0/r_g) + \tan^{-1}(\ell\omega_0/r)$, $s_g^* := (p_g^*, q_g^*)$ and $\hat{s}_g^* := s_g^* / \|s_g^*\|$, $s_f^* := (p_f^*, q_f^*)$ and $\hat{s}_f^* := s_f^* / \|s_f^*\|$.

The proof is given in Appendix A. Observe that the consistent reference specifications (45)-(46) can conceptually also be used as feedforward ac voltage and power control. Figure 5 represents the overall block diagram of the feedback controls (3), (5), and the feedforward controls (45) and (46).

If the assumption $|\theta - \theta_r| < \pi$ in Proposition 5 is not met, then according to (44) the RHS of (43) equals a 2π -periodic switching signal

$$u_{sw} := \text{sgn}(\cos(\tilde{\theta}/2)) \sin(\tilde{\theta}/2), \quad (47)$$

where $\tilde{\theta} := \theta - \theta_r$. Remark 9 explains the implications of (47) for the closed-loop dynamics (7).

Remark 9 (Switching feedback and angle invariance)

The following comments are in order:

First, the feedback u_{sw} in (47) is 2π -periodic since the implicit angle information in (43) (that is embedded in $\psi(\theta_r)$ and $\psi(\theta)$) is confined to \mathbb{S}^1 due to 2π -periodicity of $\psi(\cdot)$.

Second, an exact implementation of $\sin(\tilde{\theta}/2)$ based on (67) with $\cos(\tilde{\theta}) = \psi(\theta_r)^\top \psi(\theta)$ (as in proof of Proposition 5) can be obtained

$$\sin(\tilde{\theta}/2) := (-1)^{\lfloor \tilde{\theta}/(2\pi) \rfloor} |\sin(\tilde{\theta}/2)|,$$

that requires 4π -periodic angle error information to construct the appropriate sign pattern. However, in practice the explicit measurement of $\tilde{\theta}$ is not possible.

Third, the sign function in (47) introduce new equilibria for the closed-loop system (7) at $\tilde{\theta} = \pm\pi$ (see Figure 6). A separate analysis reveals the unstable nature of these equilibria that divide \mathbb{M} into two regions with switched subsystems i.e.,

$$\dot{x} = \begin{cases} f(x, u) & x \in]-\pi, \pi[\times \mathbb{R}^8, \\ f(x, -u) & x \in]-2\pi, -\pi[\cup]\pi, 2\pi[\times \mathbb{R}^8, \end{cases} \quad (48)$$

where $f(x, u)$ denotes the vector field (7) with $u := \sin(\tilde{\theta}/2)$. An analysis similar to Section III, verifies the AGAS of the second subsystem i.e., $\dot{x} = f(x, -u)$, $x \in \mathbb{X}$ w.r.t. x_u^* in (9). Thus, if $x(t)$ hits the switching surface $\Omega_{sw} := \{x \in \mathbb{X} : |\tilde{\theta}| = \pi\}$ it triggers the switch between the subsystems in (48) that are individually AGAS w.r.t. either x_s^* or x_u^* . The analysis of switched system (48) requires a separate study outside the scope of this paper.

Finally, we note that if $\eta = 0$ in (5), then $\dot{\theta} = -\gamma u_{sw}$ and $\mathcal{L}_{\tilde{\theta}} := \{\theta \in \mathbb{S}^1 : |\tilde{\theta}| < \pi\}$ is invariant under the flow defined by $\dot{x} = f(x, u_{sw})$. Thus, if $\theta(0) \in \mathcal{L}_{\tilde{\theta}}$, $x(t)$ never reach Ω_{sw} .

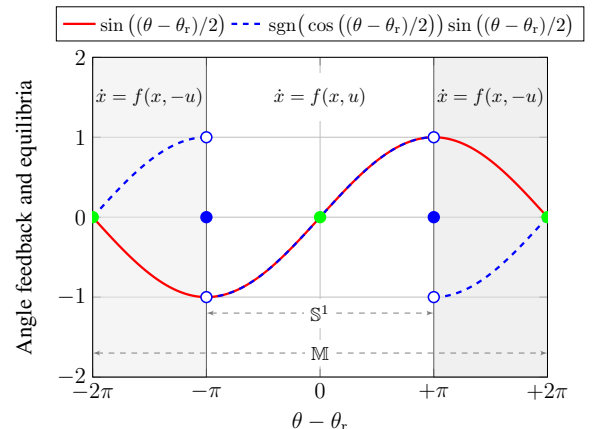


Fig. 6: Illustration of the angle feedback in (5) and the implementation (47). The implementation introduces two new equilibria (in blue) aside the existing ones (in green) in \mathbb{M} .

Remark 10 presents an alternative angle feedback that, in theory, can be incorporated in HAC (5).

Remark 10 (A globally stabilizing feedback control)
In the spirit of hybrid angle control, an alternative to (5) is

$$\omega_c := \omega_0 + \eta(v_{dc} - v_{dc,r}) - \gamma \tan^{-1}(\theta - \theta_r). \quad (49)$$

Under (49) the closed-loop system (7) is not periodic in angle and its solutions evolve in \mathbb{R}^9 . If $v_{dc}^* = v_{dc,r}$ (see Theorem 1) the unique angle equilibrium is identified by $\gamma \tan^{-1}(\theta^* - \theta_r) = 0$. Moreover, if $\mathcal{S}(\tilde{\theta})$ in Lyapunov function (15) is replaced by

$$\underline{\mathcal{S}}(\tilde{\theta}) = \int_0^{\tilde{\theta}} \tan^{-1}(s) ds = \tilde{\theta} \tan^{-1}(\tilde{\theta}) - \frac{1}{2} \ln(1 + \tilde{\theta}^2), \quad (50)$$

a similar analysis as in the Theorem 2 uncovers the global asymptotic stability (rather than AGAS) of the unique equilibrium on the basis of Lyapunov's direct method. Nonetheless, it is not clear how to construct $\tan^{-1}(\tilde{\theta})$ from $\psi(\theta)$ and $\psi(\theta_r)$ in Propositions 5 and 6.

B. HAC Power-Frequency Droop Behavior

In what follows, we consider the converter-COI closed-loop dynamics (25) that allows frequency droop which is hindered when considering the IB grid model. Recall that the existence of equilibria $\underline{\Omega}^*$ in (27) is guaranteed if $v_{dc}^* = v_{dc,r}$ and $\omega^* = \omega_0$. These assumptions can be met by appropriate choice of i_r and T_m in (25b) and (25g). For the sake of argument, assume that i_r and T_m are not consistent with the assumptions or the system is subject to disturbances, then the dc voltage and frequency converge to different equilibria $v_{dc,x}$ and ω_x . Hence, by (25a) the relative angle settles at a different equilibrium $\theta_x \neq \theta_r$. The drift from desired references is also reflected in the ac quantities.

Inspired by [16, Prop. 5], in Proposition 7 below we derive the droop slope that relates the active power and frequency at an arbitrary equilibrium. More precisely, for an operating frequency $\omega_x \in \mathbb{R}_{>0}$, the power-frequency linear sensitivity factor (also termed *droop*) is defined by $d_{p-\omega} := \partial p_{net,x} / \partial \omega_x$; see Figure 1 and the Subsection II-C for the definition of $p_{net,x}$.

Proposition 7 (Power-frequency droop slope)

Consider system (25), the power-frequency droop slope at an equilibrium with frequency ω_x and dc voltage $v_{dc,x}$ equals

$$d_{p-\omega} = - \left(\frac{2G_{dc}}{\eta^2} \right) \omega_x + \left(\frac{\eta i_0 + 2G_{dc} \beta_{\theta_x}}{\eta^2} \right), \quad (51)$$

where $G_{dc} := \kappa + g_{dc}$, $i_0 := i_r + \kappa v_{dc,r}$, $\beta_{\theta_x} := \omega_0 - \eta v_{dc,r} - \gamma \sin((\theta_x - \theta_r)/2)$, and θ_x is equilibrium relative angle.

The proof is given in Appendix A.

Remark 11 (Comments on droop slope)

With the particular choice of $\eta = \omega_0 / v_{dc,r}$ (see Remark 3) the angle term in (51) simplifies to $\beta_{\theta_x} = -\gamma \sin((\theta_x - \theta_r)/2)$. Furthermore, assuming $\theta_x - \theta_r$ is sufficiently small such that $2G_{dc} \beta_{\theta_x} / \eta^2$ is negligible compared to the other terms in (51) yields an approximation of $d_{p-\omega}$ that is

$$d_{p-\omega} \approx - \left(\frac{2G_{dc}}{\eta^2} \right) \omega_x + \left(\frac{i_0}{\eta} \right) \quad (52)$$

and coincides with the droop slope of the standard matching control [16, Prop. 5]. We close by remarking that in a multi-converter network, the ratio of droop slopes determines the proportional power-sharing among the converters.

VI. NUMERICAL EXAMPLES

In this section, we consider the closed-loop dynamics of the converter-COI system described in the Section IV-A with parameters in Table I. The converter parameters are taken from [2, Table 1] (that correspond to a commercial device). In the following, we verify the convergence of closed-loop dynamics (25) and the performance of current-limiting control (36). Moreover, we investigate the influence of HAC on the frequency performance. We remind the reader that the numerical examples in MATLAB/Simulink environment are publicly available [27].

A. Convergence of Random Initial Conditions

Consider the closed-loop dynamics of the converter-COI system (25) with angle feedback implementation (47) and parameters in Table I. Figure 7 illustrates the time-evolution of θ and all per-unit-normalized Euclidean states y_j / y_j^* for $j = 1, \dots, 9$ starting from three different initial conditions. Note that since $\theta_r = 0$, Figure 7 also depicts the converter angle synchronization with that of the COI grid model. Although depending on the initial value $\underline{x}(0)$, θ converges to either θ_r or $\theta_r \pm 2\pi$ (see Remark 9), \underline{y}^* is unique (due to its 2π -periodicity in angle). The fast convergence of angle and dc voltage are underpinned by relatively large γ/η ratio and κ . In contrast, the oscillatory behavior of the ac states are due to the negligible physical damping r , g , r_g and the fact that their dynamics are influenced by the sluggish COI frequency (via the impedance and admittance matrices in (25d)-(25f)). Moreover, the slow convergence of frequency is because of the fact that – from practical perspective – $\omega(0)$ is far from ω^* (cf. the convergence timescale of the initial condition with $\omega(0)$ close to ω^* (red trajectories) and the evolution of other initial states). Nonetheless, with a sufficiently large D and γ (see stability condition (28)) the asymptotic convergence of trajectories is guaranteed under HAC.

B. Current-Limiting Control Performance

Consider the system in previous example in combination with the current-limiting control (36) with Δ_μ as in Propo-

TABLE I: The parameters of converter-COI system (25).

converter model parameters and nominal values		
$S_{rc} = 0.5$ [MVA]	$v_r = 816.4$ [V]	$\omega_0 = 2\pi 50$ [rad/s]
$c_{dc} = 0.008$ [F]	$\ell = \ell_g = 200$ [μ H]	$c = 300$ [μ F]
$r = r_g = 0.001$ [Ω]	$g_{dc} = g = 0.001$ [Ω^{-1}]	$\tau_{dc} = 50$ [ms]
center of inertia model parameters		
$S_{r,g} = 5$ [MVA]	$H = 5$ [s]	$D = 100$
control parameters and reference values		
$\theta_r = 0$	$i_{dc,r} = 0$	$v_{dc,r} = 3v_r$
$\eta = 0.01$	$\gamma = 10000$	$\kappa = 2$
$\mu_r = 2v_r/v_{dc,r}$	$b = v_r/\omega_0$	$T_m = D\omega_0$

sition 3 where $\beta = 0.25$, $i_{th} = 1.25$ pu, and $D_{min} = 0.01$. In what follows, we consider a balanced three-phase-to-ground fault (see [45, Sec. 3.7] for the fault modeling) at the filter capacitance node in Figure 1 driving $\|v\| \rightarrow 0$ and $\mathcal{D} \rightarrow 0$. Figure 8 shows that the current-limiting control (36) (by an immediate reduction of the constant reference μ_r) effectively limits the post-fault current magnitude that aggressively exceeds i_{th} under constant modulation magnitude (that in practice trips the converter protection mechanisms). It is noteworthy that Δ_μ also significantly reduces the magnitude of oscillations in dc voltage (cf. to the case with constant modulation magnitude).

C. HAC Influence on Frequency Performance

In this example, we consider the converter-COI closed-loop system (25) with $\eta = \omega_0/v_{dc,r} = 0.128$ which renders the dc term in HAC identical to the standard matching control (see Remark 3 and [16]). Initially, it is assumed that $\gamma = 0$. Then, $\kappa = 5$ in (25b) and $D = 300$ (25g) are selected such that the converter and COI grid model exhibit equal post-contingency load-sharing (i.e., equal increase or decrease in their active power injections). In this example, the contingency is an active power load disturbance that is sized to $0.5S_{r,c}$ and is modeled by connecting a constant impedance Z_{load} in parallel connection with the ac-side capacitance in Figure 1. Figure 9

illustrates the post-contingency evolution of COI frequency (in Hertz) for different γ values. Figure 9 suggests that HAC by the means of its angle feedback in (5) significantly improves the frequency response of the standard matching control. This improvement is more tangible in the RoCoF performance metric [7, Sec. III-A] i.e.,

$$|\dot{\omega}| := \frac{|\omega(t_0 + T) - \omega(t_0)|}{T}, \quad (53)$$

where t_0 denotes the time when the disturbance is applied and T denotes the RoCoF approximation time horizon. Figure 10 shows that the RoCoF exponentially and drastically decreases as γ increases. In other word, the angle feedback of the HAC (5) serves as a remedy for the suboptimal matching control RoCoF performance (see [2, Fig. 11] for a comparison). The pure matching control senses the load disturbance (and accordingly modifies the angle dynamics) once its aftermath is propagated to the dc voltage dynamics through filter current dynamics. However, HAC with its multi-variable nature that includes both dc and ac feedback reacts to the disturbance on a slightly faster timescale that, in our opinion, explains its enhanced frequency response.

VII. SUMMARY AND OUTLOOK

In this paper, we introduced a new grid-forming control termed hybrid angle control (HAC) (5). We formally estab-

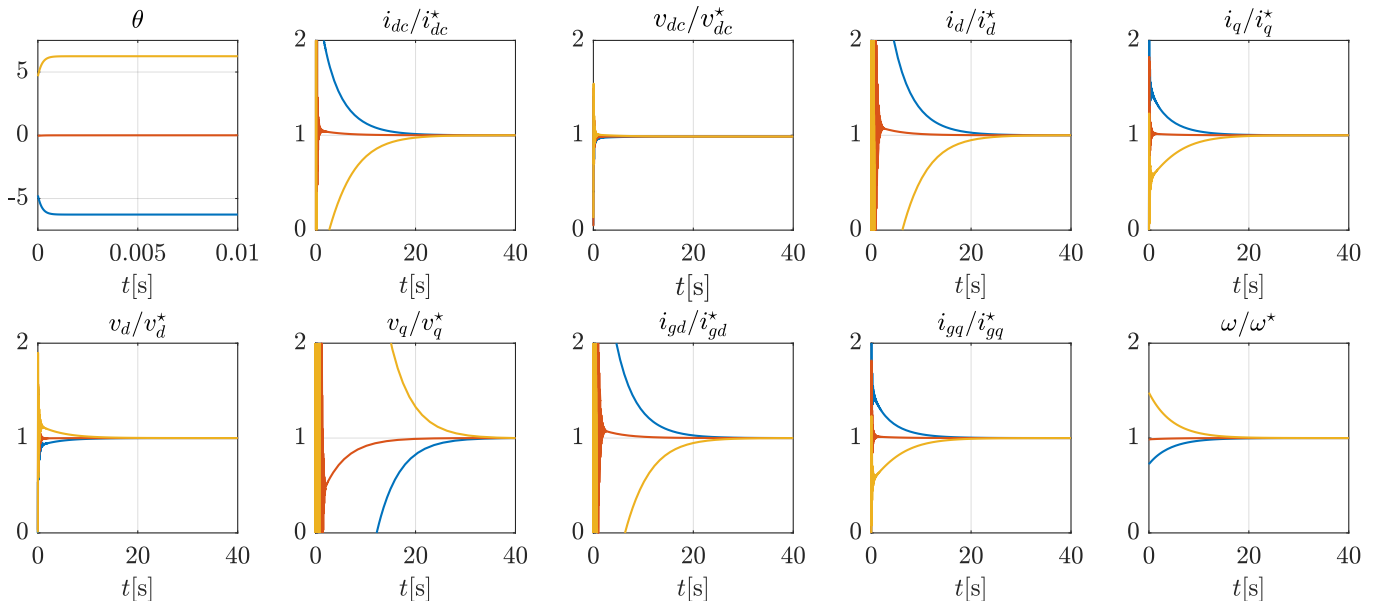


Fig. 7: Per-unit-normalized trajectories of the closed-loop system (25) with the HAC implementation in Proposition 5, parameters in Table I and three different initial conditions.

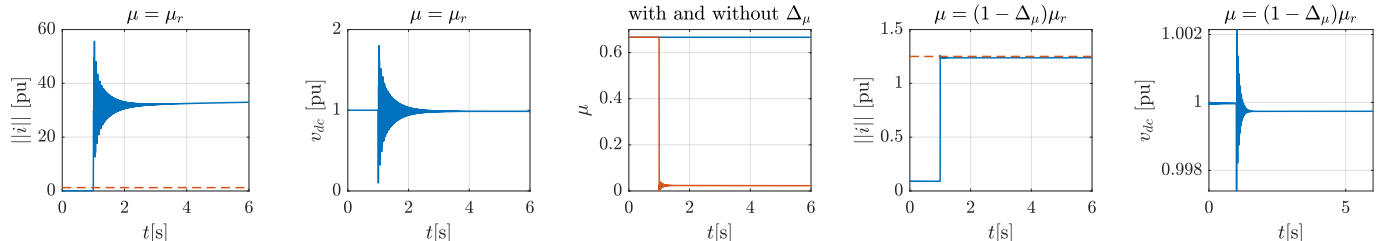


Fig. 8: Filter current, dc voltage, and modulation magnitude time-series of (25) following a three-phase-to-ground fault with and without current-limiting control (36) in per-unit system according to [29, App. B].

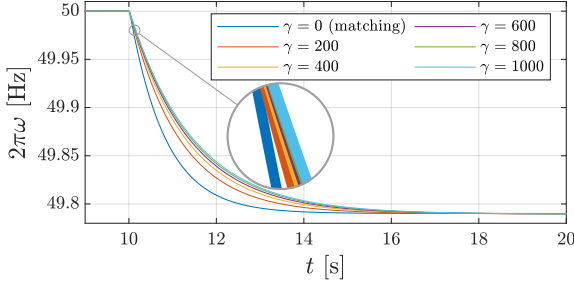


Fig. 9: Post-contingency frequency evolution of (25) for different HAC tuning.

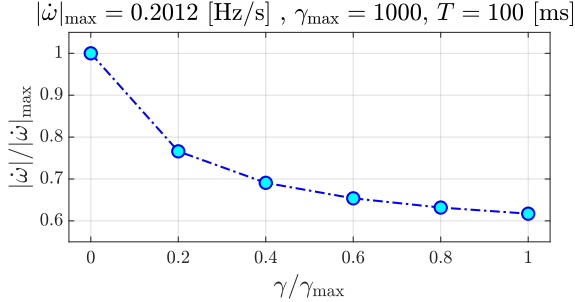


Fig. 10: Post-contingency normalized RoCoF for different HAC tuning corresponding to the frequency time-series in Figure 9.

lished the existence, uniqueness, and almost global stability of the closed-loop equilibria under mild parametric conditions. We extended the stability guarantees of HAC by considering grid dynamics and synthesized a new current-limiting control to account for the converter's safety constraints. Furthermore, a practical implementation of HAC, its intrinsic power-frequency droop behavior, and a feedforward ac voltage and power control were discussed. Last, the performance of control proposals (5) and (39) was investigated with numerical examples. Our future works will include, 1) stability analysis of interconnected converters under HAC, 2) exploring the dynamic response of the HAC and comparing its performance and robustness w.r.t. the other control techniques, and 3) investigating the compatibility of proposed current-limiting control with different grid-forming control strategies.

APPENDIX

A. Proof of Technical Results

Proof of Proposition 2. Consider the shorthand $\dot{x} = f(x)$ for (7) and let $J_f(x)$ be the Jacobian of $f(x)$, then $\det(J_f(x)) = \det(H(x))/\tau_{dc}c_{dc}(\ell c l_g)^2$ where $H(x) = \begin{pmatrix} H_{11} & H_{12} \\ H_{21} & H_{22} \end{pmatrix} :=$

$$\begin{pmatrix} -\frac{\gamma}{2} \cos\left(\frac{\theta - \theta_r}{2}\right) & 0 & \eta & 0_2^\top & 0_2^\top & 0_2^\top \\ 0 & -1 & -\kappa & 0_2^\top & 0_2^\top & 0_2^\top \\ -\frac{\partial m(\theta)}{\partial \theta} i & 1 & -g_{dc} & -m(\theta)^\top & 0_2^\top & 0_2^\top \\ v_{dc} \frac{\partial m(\theta)}{\partial \theta} & 0_2 & m(\theta) & -Z & -I & 0_{2 \times 2} \\ 0_2 & 0_2 & 0_2 & I & -Y & -I \\ 0_2 & 0_2 & 0_2 & 0_{2 \times 2} & I & -Z_g \end{pmatrix}.$$

Evaluating H_{11} at x_u^* in (9) results in $H_{11} = \begin{pmatrix} \gamma/2 & 0 \\ 0 & -1 \end{pmatrix}$ which is invertible for $\gamma > 0$. Thus, the overall determinant is

$$\det(H(x_u^*)) = \det(H_{11}) \det(H_{22} - H_{21}H_{11}^{-1}H_{12}). \quad (54)$$

Define $K := H_{22} - H_{21}H_{11}^{-1}H_{12} =$

$$\begin{pmatrix} -G_{dc} + \left(\frac{2\eta}{\gamma}\right) \frac{\partial m(\theta)}{\partial \theta} \Big|_{\theta=\theta_r} i^* & -m(\theta_r)^\top & 0_2^\top & 0_2^\top \\ m(\theta_r) - \left(\frac{2\eta v_{dc}^*}{\gamma}\right) \frac{\partial m(\theta)}{\partial \theta} \Big|_{\theta=\theta_r} & -Z & -I & 0_{2 \times 2} \\ 0_2 & I & -Y & -I \\ 0_2 & 0_{2 \times 2} & I & -Z_g \end{pmatrix}$$

where $G_{dc} := g_{dc} + \kappa$ and consider the symmetric part of K i.e., $K_S := (1/2)(K + K^\top)$. Next, we show that $K_S < 0$ under (12). Schur complements analysis yields that $K_S < 0$ iff

$$\frac{2\eta\mu_r\gamma}{G_{dc}} \frac{\partial \psi(\theta)}{\partial \theta} \Big|_{\theta=\theta_r} i^* + \frac{(\eta\mu_r v_{dc}^*)^2}{rG_{dc}} < \gamma^2. \quad (55)$$

We apply the identity (66) to the first term on the RHS of (55)

$$\begin{aligned} 2\mu_r \frac{\partial \psi(\theta)}{\partial \theta} \Big|_{\theta=\theta_r} i^* &\leq \left\| \frac{\partial \psi(\theta)}{\partial \theta} \Big|_{\theta=\theta_r} \right\|^2 + (\mu_r \|i^*\|)^2 \\ &= 1 + (\mu_r \|i^*\|)^2. \end{aligned} \quad (56)$$

Subsequently, taking into account the bound in (56), if

$$\frac{\eta\gamma}{G_{dc}} + \frac{\eta\gamma(\mu_r \|i^*\|)^2}{G_{dc}} + \frac{(\eta\mu_r v_{dc}^*)^2}{rG_{dc}} < \gamma^2, \quad (57)$$

then (55) is satisfied. Further, dividing (57) by γ results in

$$\frac{\eta}{\bar{\beta}g_{dc}} + \frac{\eta(\mu_r \|i^*\|)^2}{\bar{\beta}g_{dc}} + \frac{\eta(\mu_r v_{dc}^*)^2}{\bar{\alpha}r} < \gamma \quad (58)$$

where $\bar{\alpha} := \gamma G_{dc}/\eta$ and $\bar{\beta} := G_{dc}/g_{dc}$. Since $\bar{\beta} > 1$ by definition (recall that $G_{dc} = \kappa + g_{dc}$), if $\bar{\alpha} > 1$ then the LHS of (58) is strictly smaller than the LHS of (12). That means if $\bar{\alpha} > 1$ then (12) implies (58). To show that $\bar{\alpha} > 1$ that equals $\gamma > \eta/\bar{\beta}g_{dc}$ consider that if (12) holds then $\gamma > \eta/g_{dc} > \eta/\bar{\beta}g_{dc}$ hence $\bar{\alpha} > 1$.

To sum up, under (12), $K_S < 0$. Thus, K has all eigenvalues in the open left half-plane. Since $\dim(K) = 7$, then $\det(K) < 0$ and by (54) $\det(H(x_u^*)) = -\gamma \det(K)/2 > 0$ which means $\det(J_f(x_u^*)) > 0$. Since $\dim(J_f(x)) = 9$, then $J_f(x_u^*)$ has at least one positive real eigenvalue. Instability of x_u^* follows from Lyapunov's indirect method [32, Th. 4.7] and its global inset has zero Lebesgue measure invoking [46, Prop. 11]. ■

Proof of Proposition 6. The power injection to the IB at equilibrium [20, Def. 2] can be expressed as

$$p_g^* = -\frac{\|v^*\|v_r(r_g \cos(\delta_{bv}^*) + \ell_g \omega_0 \sin(\delta_{bv}^*))}{r_g^2 + (\ell_g \omega_0)^2}, \quad (59a)$$

$$q_g^* = -\frac{\|v^*\|v_r(\ell_g \omega_0 \cos(\delta_{bv}^*) - r_g \sin(\delta_{bv}^*))}{r_g^2 + (\ell_g \omega_0)^2}, \quad (59b)$$

where $\delta_{bv}^* := \theta_b^* - \theta_v^*$ and $\theta_v^* = \tan^{-1}(v_q^*/v_d^*)$. Taking into account the line loss and the power associated with the shunt element, we can compute p_f^* and q_f^* (see Figure 1) by

$$p_f^* = p_g^* + \left(\frac{r_g}{r_g^2 + (\ell_g \omega_0)^2} + g \right) \|v^*\|^2,$$

$$q_f^* = q_g^* + \left(\frac{\ell_g \omega_0}{r_g^2 + (\ell_g \omega_0)^2} - c\omega_0 \right) \|v^*\|^2.$$

Note that p_f^* and q_f^* are also expressed by

$$p_f^* = -\frac{\|v_s^*\| \|v^*\| (r \cos(\delta_{vc}) + \ell \omega_0 \sin(\delta_{vc}))}{r^2 + (\ell \omega_0)^2}, \quad (60a)$$

$$q_f^* = -\frac{\|v_s^*\| \|v^*\| (\ell \omega_0 \cos(\delta_{vc}) - r \sin(\delta_{vc}))}{r^2 + (\ell \omega_0)^2}, \quad (60b)$$

where $\delta_{vc} := \theta_v^* - \theta_c^*$ and $\|v_s^*\| := \mu^* v_{dc}^*$ denotes the equilibrium voltage magnitude before the filter inductor.

Consider the shorthand $\det(Z_g) = r_g^2 + (\ell_g \omega_0)^2$, and let us define $\vartheta_g := \tan^{-1}(\ell_g \omega_0 / r_g)$, $\sin(\vartheta_g) := \ell_g \omega_0 / \sqrt{\det(Z_g)}$, and $\cos(\vartheta_g) := r_g / \sqrt{\det(Z_g)}$. Then, (59) is equivalent to

$$s_g^* = -\|s_g^*\| R(\vartheta_g) \psi(\theta_v^* - \theta_b^*) = -\|s_g^*\| \psi(\theta_v^* + \vartheta_g - \theta_b^*),$$

where $\|s_g^*\| = v_r \|v^*\| / \sqrt{\det(Z_g)}$ and subsequently, $\hat{s}_g^* = -\psi(\theta_v^* + \vartheta_g - \theta_b^*)$. Similarly, define $\vartheta_f := \tan^{-1}(\ell \omega_0 / r)$, then (60) is equivalent to

$$s_f^* = -\|s_f^*\| R(\vartheta) \psi(\theta_c^* - \theta_v^*) = -\|s_f^*\| \psi(\theta_c^* + \vartheta - \theta_v^*),$$

where $\|s_f^*\| = \|v_s^*\| \|v^*\| / \sqrt{\det(Z)}$. Thus, $\hat{s}_f^* = -\psi(\theta_c^* + \vartheta - \theta_v^*)$. By the means of (69) and (70)

$$\left(\hat{s}_g^{*\top} \begin{pmatrix} +1 & 0 \\ 0 & -1 \end{pmatrix} \hat{s}_f^*, \hat{s}_g^{*\top} \begin{pmatrix} 0 & +1 \\ +1 & 0 \end{pmatrix} \hat{s}_f^* \right) = \psi(\theta_c^* - \theta_b^* + \delta)$$

and subsequently, $R(\delta)^\top \psi(\theta_c^* - \theta_b^* + \delta) = \psi(\theta^*)$.

Thus, $\psi(\theta_r)$ that is uniquely defined by (45) coincides with the solution of power flow equations, i.e., $\psi(\theta_r) = \psi(\theta^*)$. To prove the second statement (46), μ^* is derived from the expression of $\|s_f^*\|$ i.e., $\mu^* = \|s_f^*\| \sqrt{\det(Z)} / v_{dc}^* \|v^*\|$, which shows μ_r defined by (46) is consistent with μ^* . ■

Proof of Proposition 7. Note that by the relative angle dynamics (25a) at equilibrium $\omega_{c,x} = \omega_x$. Multiply (25c) at equilibrium by $v_{dc,x}$

$$i_{dc,x} v_{dc,x} - g_{dc} v_{dc,x}^2 - p_{net,x} = 0,$$

and replace $v_{dc,x}$ with the expression from (5), that is, $v_{dc,x} = (\omega_x - \beta_{\theta_x}) / \eta$ which results in

$$p_{net,x} = \frac{i_{dc,x} (\omega_x - \beta_{\theta_x})}{\eta} - \frac{g_{dc} (\omega_x - \beta_{\theta_x})^2}{\eta^2}. \quad (61)$$

Replacing $i_{dc,x}$ from (7b) at equilibrium results in

$$p_{net,x} = \frac{i_0 (\omega_x - \beta_{\theta_x})}{\eta} - \frac{(\kappa + g_{dc}) (\omega_x - \beta_{\theta_x})^2}{\eta^2}. \quad (62)$$

Hence, (51) directly follows by linearizing (62) w.r.t. ω_x . ■

B. Coordinate Transformations and Identities

1) $\alpha\beta$ -coordinates: for a three-phase quantity $z_{abc} := (z_a, z_b, z_c) \in \mathbb{R}^3$ that is balanced i.e., $z_a + z_b + z_c = 0$ the magnitude preserving Clarke transformation is defined by

$$z_{\alpha\beta} = (z_\alpha, z_\beta) := C z_{abc} = \frac{2}{3} \begin{pmatrix} 1 & -\frac{1}{2} & -\frac{1}{2} \\ 0 & \frac{\sqrt{3}}{2} & -\frac{\sqrt{3}}{2} \end{pmatrix} z_{abc}. \quad (63)$$

2) *Polar coordinates*: the transformation from Cartesian to polar coordinates i.e., $\mathcal{P} : \mathbb{R}^2 \setminus \{0\} \rightarrow \mathbb{R}_{>0} \times \mathbb{S}^1$ is

$$(\|z\|, \theta_z) = \mathcal{P}(z) := \left(\sqrt{z_1^2 + z_2^2}, \tan^{-1} \frac{z_2}{z_1} \right). \quad (64)$$

Moreover, the inverse transformation is given by

$$(z_1, z_2) = \mathcal{P}^{-1}(\|z\|, \theta_z) := \|z\| \psi(\theta_z). \quad (65)$$

Note that the polar coordinates are well-defined for the entire Cartesian space except the origin since $\mathcal{P}(0)$ is not unique.

Lemma 1 (Algebraic and trigonometric identities)

For $a, b \in \mathbb{R}^2$, $\epsilon \in \mathbb{R}_{>0}$ and $\varphi, \phi \in \mathbb{S}^1$ the followings hold

$$\pm a^\top b \leq \epsilon^2 \|a\|^2 + \frac{1}{4\epsilon^2} \|b\|^2, \quad (66)$$

$$\sin^2 \frac{\varphi}{2} = (1 - \cos \varphi) / 2, \quad (67)$$

$$\cos^2 \frac{\varphi}{2} = (1 + \cos \varphi) / 2, \quad (68)$$

$$\sin(\varphi \pm \phi) = \sin(\varphi) \cos(\phi) \pm \cos(\varphi) \sin(\phi), \quad (69)$$

$$\cos(\varphi \pm \phi) = \cos(\varphi) \cos(\phi) \mp \sin(\varphi) \sin(\phi). \quad (70)$$

REFERENCES

- [1] F. Milano, F. Dörfler, G. Hug, D. J. Hill, and G. Verbi, "Foundations and challenges of low-inertia systems," in *Power Systems Computation Conference (PSCC)*, 2018.
- [2] A. Tayyebi, D. Gro, A. Anta, F. Kupzog, and F. Drfler, "Frequency stability of synchronous machines and grid-forming power converters," *IEEE Trans. Emerg. Sel. Topics Power Electron.*, vol. 8, no. 2, pp. 1004–1018, 2020.
- [3] U. Markovic, O. Stanojev, E. Vrettos, P. Aristidou, and G. Hug, "Understanding stability of low-inertia systems," 2019, Preprint available at <http://engrxiv.org/jwzrq>.
- [4] Q. Peng, Q. Jiang, Y. Yang, T. Liu, H. Wang, and F. Blaabjerg, "On the stability of power electronics-dominated systems: challenges and potential solutions," *IEEE Trans. Ind. Appl.*, vol. 55, no. 6, pp. 7657–7670, 2019.
- [5] A. Crivellaro, A. Tayyebi, C. Gavriluta, D. Groß, A. Anta, F. Kupzog, and F. Dörfler, "Beyond low-inertia systems: Massive integration of grid-forming power converters in transmission grids," in *IEEE PES General Meeting*, 2020, To appear, preprint available at <https://arxiv.org/abs/1911.02870>.
- [6] J. Fang, H. Li, Y. Tang, and F. Blaabjerg, "On the inertia of future more-electronics power systems," *IEEE Trans. Emerg. Sel. Topics Power Electron.*, vol. 7, no. 4, pp. 2130–2146, 2018.
- [7] B. K. Poolla, D. Gro, and F. Drfler, "Placement and implementation of grid-forming and grid-following virtual inertia and fast frequency response," *IEEE Trans. Power Syst.*, vol. 34, no. 4, pp. 3035–3046, 2019.
- [8] A. Tayyebi, F. Dörfler, F. Kupzog, Z. Miletic, and W. Hribernik, "Grid-forming converters – inevitability, control strategies and challenges in future grid applications," in *CIREC Workshop*, 2018.
- [9] M. Chandorkar, D. Divan, and R. Adapa, "Control of parallel connected inverters in standalone AC supply systems," *IEEE Trans. Ind. Appl.*, vol. 29, no. 1, pp. 136–143, 1993.
- [10] J. W. Simpson-Porco, F. Dörfler, and F. Bullo, "Synchronization and power sharing for droop-controlled inverters in islanded microgrids," *Automatica*, vol. 49, no. 9, pp. 2603–2611, 2013.

- [11] Q. C. Zhong and G. Weiss, "Synchronverters: Inverters that mimic synchronous generators," *IEEE Trans. Ind. Electron.*, vol. 58, no. 4, pp. 1259–1267, 2011.
- [12] S. D'Arco, J. A. Suul, and O. B. Fosso, "A virtual synchronous machine implementation for distributed control of power converters in smart grids," *Electric Power Systems Research*, vol. 122, pp. 180–197, 2015.
- [13] I. Cvetkovic, D. Boroyevich, R. Burgos, C. Li, and P. Mattavelli, "Modeling and control of grid-connected voltage-source converters emulating isotropic and anisotropic synchronous machines," in *IEEE Workshop on Control and Modeling for Power Electronics (COMPEL)*, 2015.
- [14] L. Huang, H. Xin, Z. Wang, K. Wu, H. Wang, J. Hu, and C. Lu, "A virtual synchronous control for voltage-source converters utilizing dynamics of dc-link capacitor to realize self-synchronization," *IEEE Trans. Emerg. Sel. Topics Power Electron.*, vol. 5, no. 4, pp. 1565–1577, 2017.
- [15] S. Curi, D. Groß, and F. Dörfler, "Control of low-inertia power grids: A model reduction approach," in *IEEE Conference on Decision and Control (CDC)*, 2017.
- [16] C. Arghir, T. Jouini, and F. Drfler, "Grid-forming control for power converters based on matching of synchronous machines," *Automatica*, vol. 95, pp. 273–282, 2018.
- [17] C. Arghir and F. Drfler, "The electronic realization of synchronous machines: Model matching, angle tracking, and energy shaping techniques," *IEEE Trans. Power Electron.*, vol. 35, no. 4, pp. 4398–4410, 2020.
- [18] B. B. Johnson, M. Sinha, N. G. Ainsworth, F. Dörfler, and S. V. Dhople, "Synthesizing virtual oscillators to control islanded inverters," *IEEE Trans. Power Electron.*, vol. 31, no. 8, pp. 6002–6015, 2015.
- [19] M. Sinha, F. Dörfler, B. B. Johnson, and S. V. Dhople, "Uncovering droop control laws embedded within the nonlinear dynamics of van der pol oscillators," *IEEE Trans. Control Netw. Syst.*, vol. 4, no. 2, pp. 347–358, 2017.
- [20] M. Colombino, D. Gro, J. Brouillon, and F. Drfler, "Global phase and magnitude synchronization of coupled oscillators with application to the control of grid-forming power inverters," *IEEE Trans. Autom. Control*, vol. 64, no. 11, pp. 4496–4511, 2019.
- [21] D. Gro, M. Colombino, J. Brouillon, and F. Drfler, "The effect of transmission-line dynamics on grid-forming dispatchable virtual oscillator control," *IEEE Trans. Control Netw. Syst.*, vol. 6, no. 3, pp. 1148–1160, 2019.
- [22] H. Yu, M. Awal, H. Tu, I. Husain, and S. Lukic, "Comparative transient stability assessment of droop and dispatchable virtual oscillator controlled grid-connected inverters," *IEEE Trans. Power Electron.*, 2020.
- [23] R. Ortega, A. van der Schaft, B. Maschke, and G. Escobar, "Interconnection and damping assignment passivity-based control of port-controlled Hamiltonian systems," *Automatica*, vol. 38, no. 4, pp. 585–596, 2002.
- [24] I. Saras, R. Ortega, and E. Panteley, "Asymptotic stabilization of nonlinear systems via sign-indefinite damping injection," in *IEEE Conference on Decision and Control (CDC)*, 2012.
- [25] N. Barabanov, J. Schiffer, R. Ortega, and D. Efimov, "Conditions for Almost Global Attractivity of a Synchronous Generator Connected to an Infinite Bus," *IEEE Trans. Autom. Control*, vol. 62, pp. 4905–4916, 2017.
- [26] S. Y. Caliskan and P. Tabuada, "Compositional Transient Stability Analysis of Multimachine Power Networks," *IEEE Trans. Control Netw. Syst.*, vol. 1, no. 1, pp. 4–14, 2014.
- [27] A. Tayyebi, "HybridAngleControl(HAC): Implementation of grid-forming hybrid angle control," Git repository, 2020, <https://github.com/ATayyebi/HybridAngleControl-HAC>.
- [28] S. P. Bhat and D. S. Bernstein, "A topological obstruction to continuous global stabilization of rotational motion and the unwinding phenomenon," *Systems & Control Letters*, vol. 39, no. 1, pp. 63–70, 2000.
- [29] A. Yazdani and R. Iravani, *Voltage-sourced converters in power systems: modeling, control, and applications*. John Wiley & Sons, 2010.
- [30] F. Milano and Á. O. Manjavacas, *Converter-Interfaced Energy Storage Systems: Context, Modelling and Dynamic Analysis*. Cambridge University Press, 2019.
- [31] G.-S. Seo, M. Colombino, I. Subotic, B. Johnson, D. Groß, and F. Dörfler, "Dispatchable virtual oscillator control for decentralized inverter-dominated power systems: Analysis and experiments," in *IEEE Applied Power Electronics Conference and Exposition (APEC)*, 2019.
- [32] H. Khalil, *Nonlinear Systems*. Prentice Hall, 2002.
- [33] A. D. Paquette and D. M. Divan, "Virtual impedance current limiting for inverters in microgrids with synchronous generators," *IEEE Trans. Ind. Appl.*, vol. 51, no. 2, pp. 1630–1638, 2015.
- [34] I. Suboti, D. Gro, M. Colombino, and F. Drfler, "A Lyapunov framework for nested dynamical systems on multiple time scales with application to converter-based power systems," 2019, Preprint available at <https://arxiv.org/abs/1911.08945>.
- [35] S. Baros, C. N. Hadjicostis, and F. O'Sullivan, "Stability analysis of droop-controlled inverter-based power grids via timescale separation," 2020, Preprint available at <https://arxiv.org/abs/2003.11934>.
- [36] J. H. Chow, Ed., *Power System Coherency and Model Reduction*. Springer, 2013, vol. 94.
- [37] D. Romeres, F. Drfler, and F. Bullo, "Novel results on slow coherency in consensus and power networks," in *European Control Conference (ECC)*, 2013.
- [38] P. W. Sauer and M. A. Pai, *Power system dynamics and stability*. Prentice hall, 1998.
- [39] A. Ulbig, T. S. Borsche, and G. Andersson, "Impact of Low Rotational Inertia on Power System Stability and Operation," *IFAC Proceedings Volumes*, vol. 47, no. 3, pp. 7290–7297, 2014.
- [40] J. Machowski, Z. Lubosny, J. W. Bialek, and J. R. Bumby, *Power system dynamics: stability and control*. John Wiley & Sons, 2020.
- [41] I. Sadeghkhani, M. E. H. Golshan, J. M. Guerrero, and A. Mehrizi-Sani, "A current limiting strategy to improve fault ride-through of inverter interfaced autonomous microgrids," *IEEE Trans. Smart Grid*, vol. 8, no. 5, pp. 2138–2148, 2016.
- [42] D. Gro and F. Drfler, "Projected grid-forming control for current-limiting of power converters," in *Allerton Conference on Communication, Control, and Computing*, 2019.
- [43] M. G. Taul, X. Wang, P. Davari, and F. Blaabjerg, "Current limiting control with enhanced dynamics of grid-forming converters during fault conditions," *IEEE Trans. Emerg. Sel. Topics Power Electron.*, vol. 8, no. 2, pp. 1062–1073, 2020.
- [44] F. Blanchini, "Set invariance in control," *Automatica*, vol. 35, no. 11, pp. 1747 – 1767, 1999.
- [45] P. Kundur, *Power system stability and control*. McGraw-hill, 1994.
- [46] P. Monzon and R. Potrie, "Local and global aspects of almost global stability," in *IEEE Conference on Decision and Control (CDC)*, 2006.



Ali Tayyebi received his BSc degree in electrical engineering from the University of Tehran, Iran in 2012. In 2014 he received his MSc degree in engineering mathematics (joint MATHMODS program) from University of L'Aquila, and University of Hamburg in Italy and Germany respectively. In 2016, he received his second MSc degree in sustainable transportation and electric power systems (joint STEPS program) from La Sapienza, University of Nottingham and University of Oviedo respectively in Italy, UK and Spain. From 2014 to 2016, he was

the recipient of EU scholarship for master studies. In 2016, he joined Austrian Institute of Technology (AIT) in Vienna, Austria as a master thesis candidate and afterward continued with AIT as research assistant. In 2017, he started his joint PhD project at AIT and Automatic Control Laboratory, Swiss Federal Institute of Technology (ETH) Zurich, Switzerland. His main research interest is the non-linear systems and control theory with applications to power system. In particular, his PhD research focuses on the design of grid-forming converter control for low-inertia power system. He has recently won the IEEE PES General Meeting 2020 best paper award.



Adolfo Anta received the Licenciatura degree from ICAI Engineering School, Madrid, Spain, in 2002, and the M.Sc. and Ph.D. degrees from the University of California, Los Angeles, CA, USA, in 2007 and 2010, respectively. From 2002 to 2005, he was a Design Engineer with EADS-Astrium and, from 2010 to 2012, he was a Postdoctoral Researcher with the Technical University of Berlin and the Max Planck Institute, Germany. From 2012 to 2018 he worked as lead researcher at GE Global Research Europe, Germany. He is currently with Austrian

Institute of Technology AIT as research engineer in Vienna, Austria. His research interests cover a wide range of control applications, in particular stability issues in power systems. Dr. Anta received the Fulbright Scholarship in 2005, the Alexander von Humboldt Fellowship in 2011, was a Finalist for the Student Best Paper Award at the IEEE Conference on Decision and Control in 2008, and received the 2010 EMSOFT Best Paper Award and the IEEE CSS George S. Axelby Award in 2011, and won the IEEE PES General Meeting 2020 best paper award.



Florian Dörfler (S09M13) Florian Drfler is an Associate Professor at the Automatic Control Laboratory at ETH Zurich. He received his Ph.D. degree in Mechanical Engineering from the University of California at Santa Barbara in 2013, and a Diploma degree in Engineering Cybernetics from the University of Stuttgart in 2008. From 2013 to 2014 he was an Assistant Professor at the University of California Los Angeles. His primary research interests are centered around control, optimization, and system theory with applications in network systems such

as electric power grids, robotic coordination, and social networks. He is a recipient of the distinguished young research awards by IFAC (Manfred Thoma Medal 2020) and EUCA (European Control Award 2020). His students were winners or finalists for Best Student Paper awards at the European Control Conference (2013, 2019), the American Control Conference (2016), the PES General Meeting (2020), and the PES PowerTech Conference (2017). He is furthermore a recipient of the 2010 ACC Student Best Paper Award, the 2011 O. Hugo Schuck Best Paper Award, the 2012-2014 Automatica Best Paper Award, the 2016 IEEE Circuits and Systems Guillemin-Cauer Best Paper Award, and the 2015 UCSB ME Best PhD award.